JCB Journal of Cell Biology

REPORT

The KIF3B/B/KAP3 tail domain specifically facilitates TRIM46 transport to the axon initial segment

Xuguang Jiang[1]*, Sotaro Ichinose[2]*, Tadayuki Ogawa[3], Kento Yonezawa[4,5], Nobutaka Shimizu[4,6], and Nobutaka Hirokawa[1,7]

Intracellular transport is essential for neuronal organization, yet how motor proteins achieve cargo selectivity remains incompletely understood. Kinesin-2 motors transport diverse cargos through the heterotrimeric KIF3/KAP3 complex, but whether variations in assembly composition contribute to functional specificity has been unclear. This study provides evidence for heterogeneity in neuronal KIF3/KAP3 assemblies, including a KIF3B-enriched, KAP3-associated population in addition to the canonical KIF3A/B/KAP3 complex. Biochemical and cellular analyses support a preferential association between this KIF3B-enriched assembly and TRIM46, a protein required for axon initial segment organization. Structural analyses further suggest that differences in tail conformation accompany distinct assembly states and may underlie cargo selectivity. Together, these findings support a model in which compositional and structural diversity within kinesin-2 complexes contributes to spatially regulated transport during neuronal development.

Introduction

Kinesin superfamily proteins (KIFs) are microtubule (MT)-dependent molecular motors that drive intracellular transport. They transport various cargos, including organelles, synaptic vesicle precursors, neurotransmitter receptors, cell signaling molecules, cell adhesion molecules, and mRNAs (Hirokawa, 1998; Hirokawa et al., 2010). KIF3, a kinesin-2 family member, forms a heterotrimeric complex that consists of KIF3A, KIF3B, and kinesin-associated protein 3 (KAP3) (Kondo et al., 1994; Yamazaki et al., 1996; Teng et al., 2005). KIF3 is essential for intraciliary transport during left/right determination (Hirokawa et al., 2009) and contributes to cell polarity (Nishimura et al., 2004), ion channel transport (Gu et al., 2006; Gu and Gu, 2010), and activity-dependent transport of neuronal cargos, including N-cadherin (Ichinose et al., 2015) and NMDA receptor NR2A (Alsabban et al., 2020).

Early quantitative analyses reported an ~1:1 stoichiometry between KIF3A and KIF3B across multiple organisms, based on purified native or recombinant complexes (Scholey, 2013), including mouse testis (Yamazaki et al., 1995), which led to the prevailing view that KIF3/KAP3 functions predominantly as a heterotrimeric complex. However, the finding that KAP3 is present at lower levels than KIF3A/B, suggests that additional organizational states may exist. To date, quantitative measurements of KIF3/KAP3 components in mammalian brain tissue have not been reported. Moreover, the subsequent identification of a brain-specific KIF3A/C complex (Muresan et al., 1998) further challenges the assumption that KIF3A and KIF3B necessarily assemble into a strictly heterodimeric core with a 1:1 stoichiometry in the mammalian brain context.

Neurons, with their long neurites, rely on efficient long-distance transport for precise protein distribution. Biophysical analyses have unveiled how KIF3 achieves this. Kinesin-2, to which KIF3 belongs, has a longer neck linker than kinesin-1, enabling superior obstacle-avoidance capability (Hoeprich et al., 2014). Protein oligomerization enhances functional diversity, particularly through hetero-oligomerization (Kumari and Yadav, 2019). In KIF3, the heterodimer exhibits a lower MT association rate than homodimers (Quinn et al., 2018), allowing multiple heterodimers to cooperate on a single vesicle (Schimert et al., 2019; Bensel et al., 2020; Jiang et al., 2025a). These insights explain KIF3-mediated long-distance transport within neurons. However, the transient nature of protein hetero-oligomers makes it difficult to elucidate their molecular mechanisms in cells (Liu and Luo, 2023), underscoring the importance of determining

---

[1]Department of Cell Biology and Anatomy, Graduate School of Medicine, The University of Tokyo, Tokyo, Japan; [2]Department of Anatomy, Graduate School of Medicine, Gunma University, Gunma, Japan; [3]Laboratory for Molecular Pathobiology, Research Center for Advanced Medical Science, Dokkyo Medical University, Tochigi, Japan; [4]Structural Biology Research Center, Photon Factory, Institute of Materials Structure Science, High Energy Accelerator Research Organization (KEK), Ibaraki, Japan; [5]Center for Digital Green-innovation, Nara Institute of Science and Technology, Nara, Japan; [6]Life Science Research Infrastructure Group, Advanced Photon Technology Division, RIKEN SPring-8 Center, Hyogo, Japan; [7]Graduate School of Medicine, Juntendo University, Tokyo, Japan.

*X. Jiang and S. Ichinose contributed equally to this paper. Correspondence to Nobutaka Hirokawa: hirokawa@m.u-tokyo.ac.jp.

Rockefeller University Press
J. Cell Biol. 2026 Vol. 225 No. 5 e202503138

https://doi.org/10.1083/jcb.202503138

their cellular distribution and stoichiometry for a deeper understanding of protein transport in neurons.

Despite the progress, our understanding of oligomerization, particularly in relation to cargo recognition by tail domains, remains limited. KIF3 transports diverse cargos and exhibits variability due to splicing variants, posttranscriptional modifications, and structural differences (Yamazaki et al., 1996; Carpenter et al., 2015; Ichinose et al., 2015; Ichinose et al., 2019). With this in mind, we examined the relationship between cargo variety and KIF3 tail composition to better understand protein distribution in neurons. Recent studies showed that the KIF3A/B/KAP3 complex binds APC through a hook-like domain formed by the KIF3A and KAP3 (Jiang et al., 2023; Jiang et al., 2025b), while a β-hairpin motif within this domain regulates motor activity by interacting with the motor domain (Webb et al., 2025). In contrast, TRIM46, a cargo transported to the axon initial segment (AIS), is likely distinct from ARM-containing cargos such as APC, which also interacts with the NMDA receptor and is targeted to dendrites (Ichinose et al., 2019; Alsabban et al., 2020).

In this study, we investigated the oligomeric state of KIF3 and its cargo recognition mechanisms. Knockdown (KD) and knockout (KO) experiments in hippocampal neurons suggested that KIF3B is required for efficient TRIM46 transport. Furthermore, immunocytochemical analysis suggested that endogenous KIF3A, KIF3B, and KAP3 do not always strictly co-localize, with KIF3B-only puncta observed specifically within axons. Biochemical analyses of mouse brain samples supported this, indicating an inconsistent distribution of KIF3A and KIF3B and suggesting the presence of a KIF3B-enriched, KAP3-associated assembly (hereafter referred to as KIF3B/B/KAP3 for simplicity). In the absence of KIF3A, this assembly may function as a cargo-binding module that preferentially associates with TRIM46 rather than previously identified ARM-containing cargos. Furthermore, small-angle X-ray scattering (SAXS) and structural analysis suggest distinct structural bases and regulatory mechanisms for KIF3B/B/KAP3 and KIF3A/B/KAP3 cargo interactions. Together, these findings extend the current understanding of the kinesin-2 complex, offering insights into how diverse oligomeric states and transport mechanisms contribute to neuronal morphogenesis and function.

Results and discussion

KIF3B contributes to TRIM46 accumulation at the AIS

As an initial step, we validated the specificity of the KIF3 antibodies in Neuro2a cells (Fig. S1, A–E). Both vector-based KD and KO strategies were employed. Because the efficiency of KIF3A KO was insufficient, anti-KIF3A was validated in KD cells, whereas anti-KIF3B was validated in KO cells to assess specificity.

To investigate the relationship between the KIF3/KAP3 complex and TRIM46, we analyzed the effects of knocking down KIF3A and KIF3B in primary hippocampal neurons. shRNA vectors were electroporated at DIV0, and immunostaining at DIV4 confirmed reduced expression of both KIF3A and KIF3B (Fig. S1, F and G). Because KIF3 turnover is 2–3 days and AIS construction is completed by DIV4, this represents the only feasible time window (Heo et al., 2018; Ichinose et al., 2019). Under these conditions, TRIM46 accumulation at the AIS was significantly shortened in KD neurons, with the strongest effect in KIF3B KD at the distribution level (Fig. 1, A–C).

To exclude off-target RNAi effects, CRISPR-based KO vectors with or without resistant KIF3B were introduced at DIV0, and successful KO and rescue were confirmed (Fig. S1, H and I). KIF3B KO neurons showed reduced AIS accumulation of TRIM46 and AnkG, which was restored by resistant KIF3B (Fig. 1, D and E). In contrast, total soma levels of TRIM46 and AnkG were unchanged, indicating that loss of KIF3B specifically impairs AIS accumulation rather than protein expression (Fig. S1, K and L). These findings indicate that KIF3B contributes to TRIM46 accumulation at the AIS.

Finally, we tested whether TRIM46 regulates KIF3B degradation. TRIM46 contains an N-terminal RING domain functioning as an E3 ubiquitin ligase, so we expressed full-length or ΔRING TRIM46 together with myc-KIF3B-His7 in Neuro2a cells. Cycloheximide (CHX) chase and ubiquitination assays showed no differences in protein stability or ubiquitination (Fig. 1, F–I). Thus, the KIF3B–TRIM46 interaction reflects KIF3B-dependent transport of TRIM46, rather than TRIM46-mediated degradation of KIF3B.

Loss-of-function analyses showed that KIF3B is required for proper accumulation of TRIM46 at the AIS. KIF3B KD or KO reduced AIS-associated TRIM46 without affecting total cellular levels, indicating a defect in subcellular transport rather than protein stability. Rescue with KO-resistant KIF3B restored TRIM46 accumulation at the AIS, confirming the specificity of this effect. These findings indicate that KIF3B contributes to TRIM46 transport during early neuronal development, consistent with the activation of TRIM46 transport at DIV4 (Ichinose et al., 2019).

KIF3 exhibits diversity in its components at the AIS

We therefore examined endogenous KIF3 components (KIF3A, KIF3B, and KAP3) at the AIS at DIV4 and found both co-localizing and independent puncta (Fig. 2 A). Quantitative distance analysis divided the puncta into short- and long-distance groups (Fig. 2 B and Fig. S1 M), suggesting that KIF3B does not always co-localize with KIF3A, and KIF3A does not always co-localize with KAP3. We further confirmed that this classification was not attributable to steric hindrance between antibodies (Fig. S1, N–Q).

To test whether the endogenous localization patterns of KIF3 proteins could be recapitulated in an overexpression system, we expressed tagged KIF3A and KIF3B and induced a rigor state with ATPγS/paclitaxel while extracting excess KIF3. Even under these conditions, non–co-localized puncta were observed at the AIS, consistent with immunocytochemistry (Fig. 2, C and D).

Finally, when compared within single cells, co-localization was consistently lower in axons than in somatodendritic regions (Fig. 2 D), and the overall mean value was also significantly reduced (Fig. 2 E). This suggests that conventional KIF3A/B heterodimers are more abundant in somatodendritic regions, whereas axons show relative enrichment of KIF3B, consistent with its role in TRIM46 transport. Thus, KIF3 dimerization may differ depending on the subcellular compartment.

These findings indicate that KIF3A and KIF3B are not exclusively present as strict heterodimers. Instead, axons show a

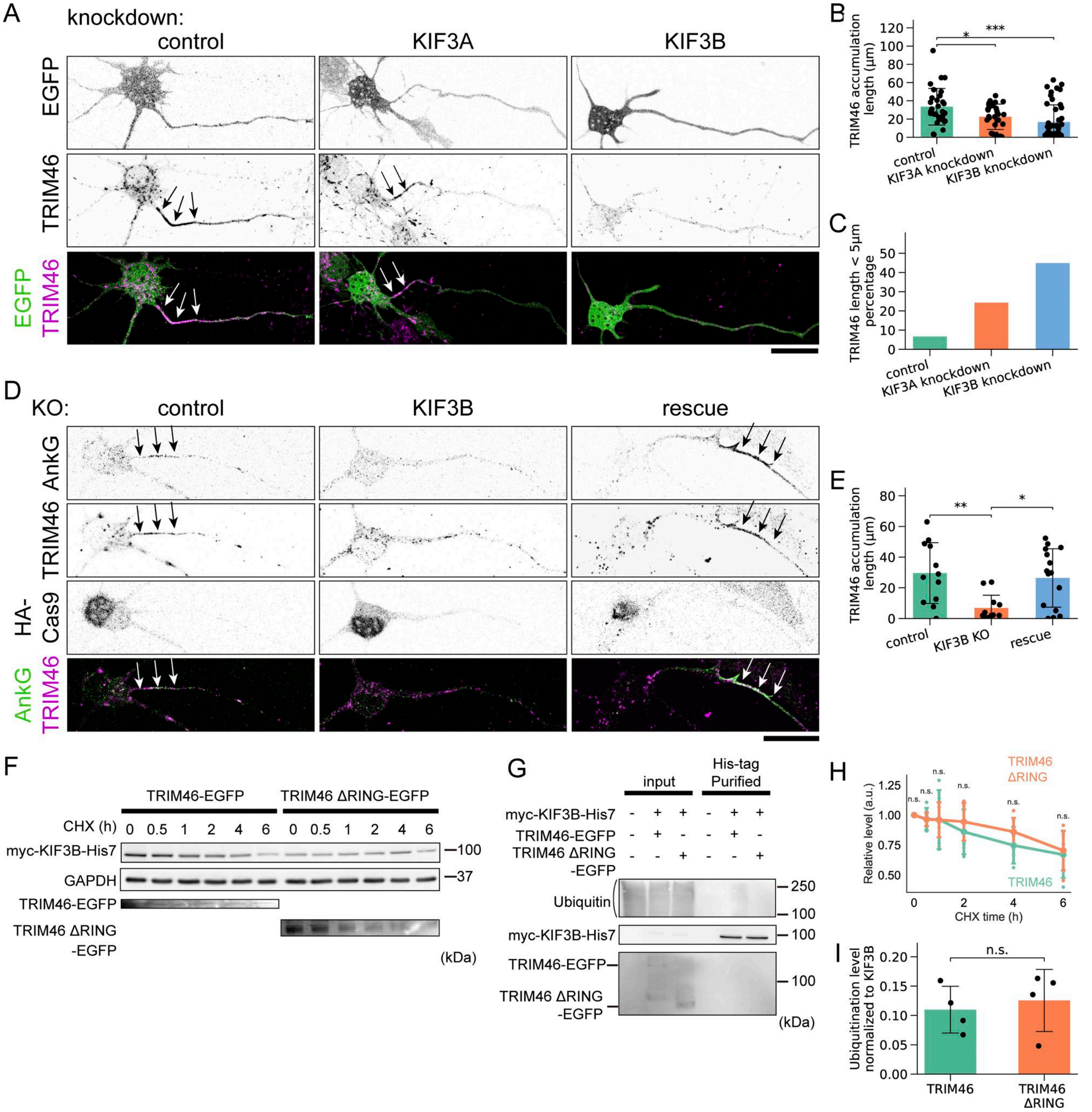

Figure 1. **KIF3B is required for TRIM46 accumulation at the AIS. (A)** Immunostaining of TRIM46 in KD neurons. Arrows indicate TRIM46 accumulation above a defined intensity threshold. Scale bar, 20 μm. **(B)** Statistical analysis of AIS length in KD experiments. Data are shown as bar graphs with mean ± SD and dot plots. One-way ANOVA followed by Tukey's post hoc test. *, P = 0.0417 (control vs KIF3A KD) and ***, P = 0.0003 (control vs KIF3B KD). *n* = 30 (control), 33 (KIF3A KD), and 49 (KIF3B KD). **(C)** Percentage of neurons with AIS length <5 μm. **(D)** Immunostaining of AnkG and TRIM46 in CRISPR-mediated KO neurons expressing HA-Cas9. Arrows indicate AnkG and TRIM46 accumulation above a defined intensity threshold. Scale bar, 20 μm. **(E)** Statistical analysis of AIS length in KO experiments. Data are shown as bar graphs with mean ± SD and dot plots. One-way ANOVA followed by Tukey's post hoc test revealed a significant difference between control and KIF3B KO (**, P = 0.0058), a significant difference between KIF3B KO and rescue (*, P = 0.013), and no significant difference between control and rescue (P = 0.8762). *n* = 12 (control), 12 (KIF3B KO), and 15 (rescue). **(F)** Western blotting of CHX chase experiments. **(G)** Western blotting of KIF3B ubiquitination. Myc-KIF3B-His7 was purified under denaturing conditions in the presence of 6 M guanidine, and ubiquitination was assessed; no marked ubiquitination was detected. **(H)** Line graph showing the results of CHX chase experiments. Protein levels of myc-KIF3B-His7 were normalized to the level at 0 h after CHX treatment (set to 1.00). At each time point, no significant difference was detected between co-transfection with full-length TRIM46 and TRIM46 ΔRING. Data are shown as line plots representing the mean ± SD, together with individual data points. P = 0.958, 0.986, 0.466, 0.224, and 0.772 for 0.5, 1, 2, 4, and 6 h, respectively, by Welch's *t* test. *n* = 5 biological replicates. **(I)** Quantification of ubiquitination. Data are shown as bar graphs with mean ± SD and dot plots. Signal intensities of ubiquitin immunoreactivity above 100 kDa were measured and normalized to myc-KIF3B-His7. No significant difference was detected between co-transfection with full-length TRIM46 and TRIM46 ΔRING. P = 0.653 by Welch's *t* test. *n* = 4 biological replicates. Source data are available for this figure: SourceData F1.

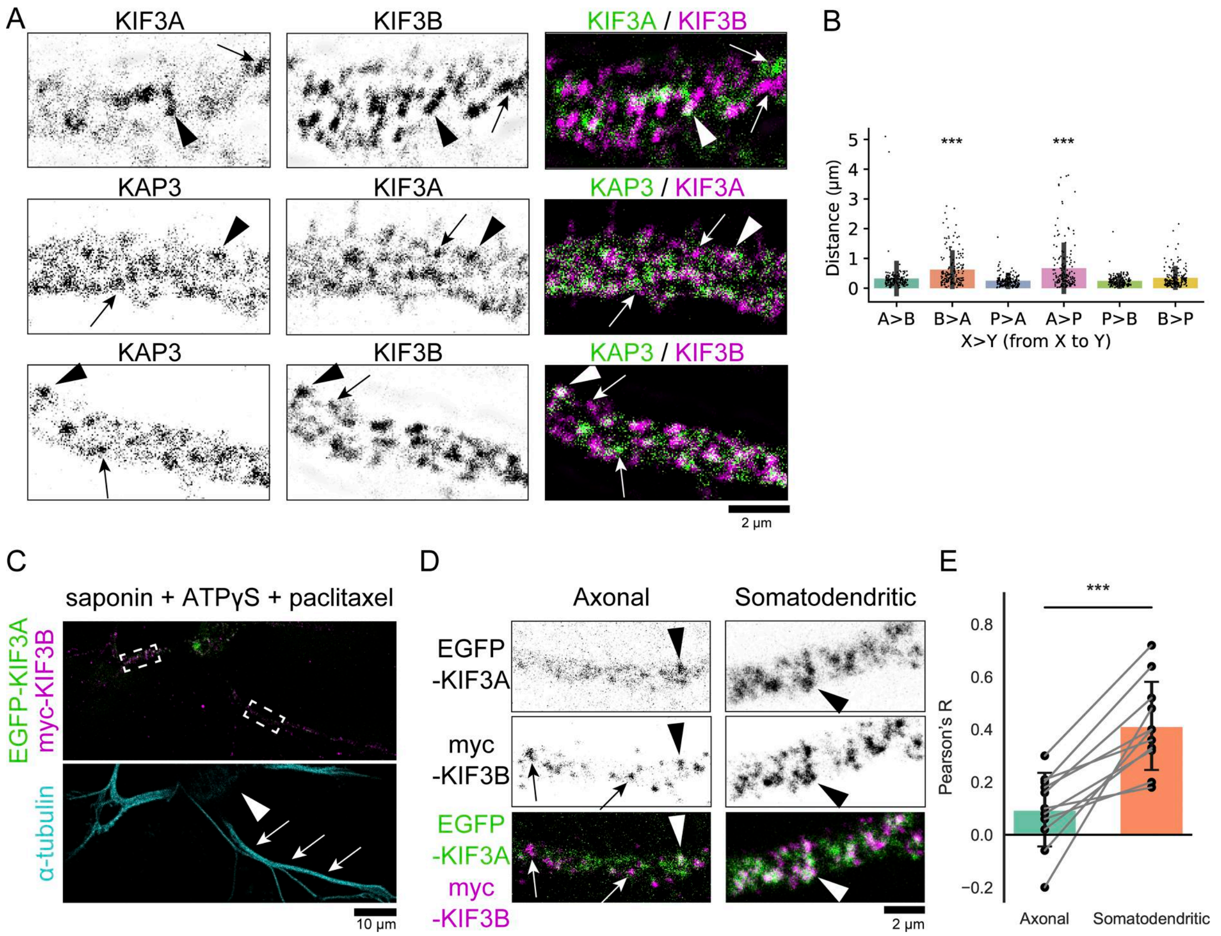

Figure 2. **KIF3 exhibits diversity in its components at the AIS. (A)** Immunostaining images of endogenous KIF3 components at proximal axon. All combination has co-localizing puncta (arrowheads) and independent puncta (arrows). Scale bar, 2 µm. **(B)** Quantification of the minimum distance between KIF3 components. Data are presented as bar graphs with mean ± SD and dot plots. Protein distance is expressed in the $X > Y$ format, representing the distance from protein X to protein Y. A: KIF3A, B: KIF3B, P: KAP3. Due to the large number of pairwise comparisons, details of the significance tests are provided in Fig. S1 M. Representative significant differences are indicated as ***($P < 0.001$). $n = 170$ for each combination, obtained by randomly sampling 10 puncta from each of 17 neurons. **(C)** Representative images showing EGFP-KIF3A (EGFP signal) and myc-KIF3B (anti-myc immunoreactivity) in individual cells under rigor conditions. To confirm neurite orientation and detect ROIs, α-tubulin was co-stained. Dashed boxes (left: somatodendritic; right: axonal) are enlarged in D. Arrowheads indicate soma, and arrows indicate axons (longest neurites). Scale bar, 10 µm. **(D)** Enlarged views. In both axonal and somatodendritic regions, co-localizing puncta of KIF3A and KIF3B (arrowheads) as well as single puncta (arrows) were observed. Notably, axonal regions showed more KIF3B-only puncta. Scale bar, 2 µm. **(E)** Statistical analysis of KIF3A and KIF3B overlap in rigor state. Data are shown as bar graphs with mean ± SD and dot plots, with data from the same cells connected by gray lines. Pearson's correlation coefficients were significantly higher in the somatodendritic region, indicating greater overlap between KIF3A and KIF3B. In contrast, overlap between KIF3A and KIF3B was reduced in the axonal region. $P = 0.0001$ by Welch's *t* test. $n = 11$ neurons.

relative enrichment of KIF3B-only assemblies, consistent with the spatial and temporal specificity of TRIM46 transport. The detection of KIF3B-only assemblies specifically under such conditions may explain why such configurations have been overlooked in previous studies.

KIF3B/B/KAP3 preferentially associates with TRIM46

We next asked whether the soluble KIF3B/B fraction has a specific function. To this end, pull-down assays were performed using GST-tagged KIF3A and KIF3B dimers, as well as their complexes with KAP3, with the mouse brain S2 fraction to probe their binding to previously reported cargoes of KIF3. As a result, while α-fodrin, APC, and β-catenin were pulled down by KIF3A/A, KIF3A/B, KIF3A/A/KAP3, and KIF3A/B/KAP3 rather than KIF3B/B and KIF3B/B/KAP3, TRIM46, which was previously found to interact with the KIF3B tail and KAP3 (Ichinose et al., 2019), exhibited preferential association with KIF3B/B/KAP3 (Fig. 3, A and B). Immunoprecipitation (IP) experiments using KIF3B and TRIM46 antibodies showed consistent results: KIF3B and KAP3, but not KIF3A, were IPed by TRIM46 antibody (Fig. 3 C).

Previous studies have suggested that KIF3A and KIF3B tightly associate as a heterodimer in brain membrane fractions (Yamazaki et al., 1995). In addition, density gradient centrifugation followed by immunoblotting of cytosolic MT-associated fractions showed comigration of KIF3A and KIF3B (Muresan et al., 1998). However, because of their similar molecular weights, the resolution of density gradient centrifugation is insufficient to determine whether these signals represent a homogeneous KIF3A/B/KAP3 complex or a mixture of multiple

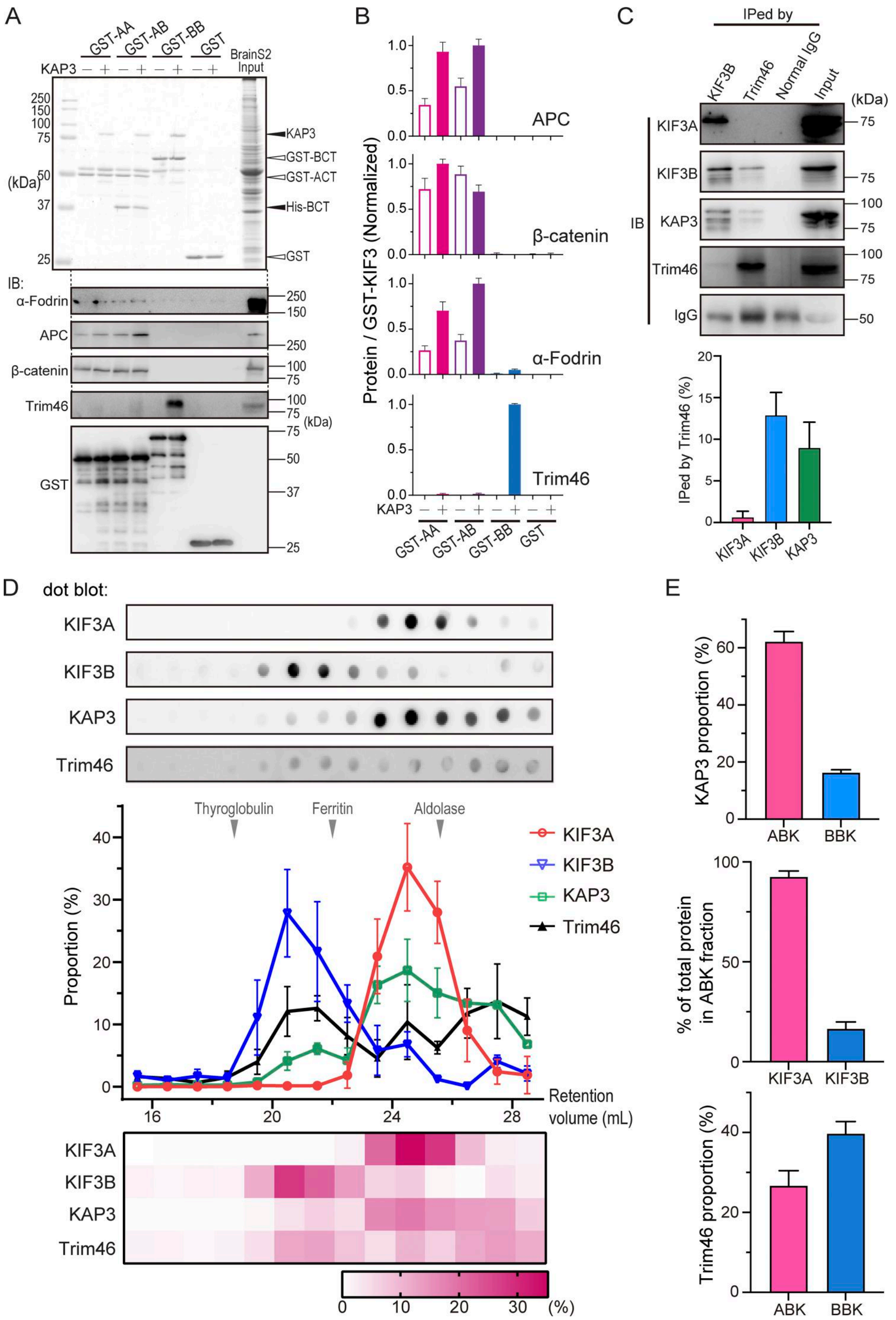

Figure 3. **KIF3/KAP3 subtypes exhibited cargo-binding specificity. (A)** Pull-down assay assessing the binding capability of different KIF3/KAP3 complexes with reported cargoes. GST-AA, GST-BB, and GST-AB indicate GST-tagged homodimeric ACT (KIF3A 481–701), homodimeric BCT (KIF3B 475–747), and heterodimeric ACT/BCT, respectively. The S2 fraction of mouse brain lysate was used as input samples, and the results were evaluated by SDS-PAGE (top panel) and western blot (bottom panel). **(B)** Quantification analysis of the western blot results in A. Data are shown as bar graphs with mean ± SD. **(C)** IP analysis using anti-KIF3B and anti-TRIM46 antibodies with the brain S2 fraction as input. Rabbit normal IgG was also used as a control. Quantitative analysis was performed on the TRIM46 antibody IP group, in which the signal intensity of the IPed fraction was quantified as a percentage of its corresponding input based on densitometric measurements. Three replicates were performed, and data are shown as bar graphs with mean ± SD. **(D)** HiRes-SEC and dot blot analyses of the mouse brain S3 fraction probing the distribution of KIF3A, KIF3B, KAP3, and TRIM46. The elution fractions from SEC were used for dot blot analysis, with the results corresponding to their retention volumes in the SEC chromatogram (left panel). Quantification analysis was performed with five replicates and is shown as a line chart and heatmap (right panel). Elution positions of molecular weight markers are indicated: thyroglobulin (669 kDa), ferritin (440 kDa), and aldolase (158 kDa). **(E)** Quantification of protein distribution. The top panel shows the proportion of KAP3 in the KIF3A/B/KAP3 (ABK, 23.5–26.5 ml) and KIF3B/B/KAP3 (BBK, 19.5–22.5 ml) peak fractions. The middle panel quantifies KIF3A and KIF3B protein levels partitioned into the ABK fraction. The bottom panel shows the Trim46 distribution in each KIF3 fraction. Data are presented as the percentage of each subunit recovered in the fractions relative to its respective total level. Bars represent mean ± SD from *n* = 3 independent experiments.

KIF3–KAP3 assemblies involving KIF3A and KIF3B in different combinations. Thus, to further confirm our findings regarding the existence of distinct KIF3/KAP3 subtypes and their cargo-binding specificity, high-resolution size-exclusion chromatography (HiRes-SEC) assays were performed using the mouse brain cytosolic (S3) fraction, without MT co-pelleting purification, to assess the native in-solution distribution of KIF3/KAP3 assemblies and their association with TRIM46. As a result, independent comigration of KIF3B and KAP3 prior to the comigration of KIF3A/B/KAP3 was observed, suggesting the independent fraction of KIF3B/B/KAP3 (Fig. 3 D and Fig. S2 A). To estimate the ratio of KIF3A/B/KAP3 and KIF3B/B/KAP3 complexes, we calculated the proportion of KAP3 at the corresponding peaks where each complex was present, since KAP3 abundance provides a reliable comparative index between these complexes based on its tight association with KIF3. The results showed that KIF3A/B/KAP3 was the major fraction, whereas KIF3B/B/KAP3 represented a minor fraction, with KIF3A/B/KAP3 being approximately three times more abundant than KIF3B/B/KAP3 (Fig. 3 E, top panel). Moreover, only ~16% of cytosolic KIF3B was found to comigrate with KIF3A in the KIF3A/B/KAP3 fraction (Fig. 3 E, middle panel). This disparity suggests either an imbalance in the total pools of KIF3A and KIF3B within the membrane-free cytosolic fraction or the potential formation of alternative complexes, such as KIF3A/C/KAP3 (Fig. 3 E, middle panel). Taken together, these findings support the presence of at least two functionally distinct KIF3/KAP3 assemblies: KIF3A/B/KAP3 and KIF3B/B/KAP3.

Importantly, TRIM46 co-eluted with KIF3B/B/KAP3 in the high–molecular weight fractions corresponding to the potential KIF3B/B/KAP3–TRIM46 complex (Fig. 3 D), exhibiting a higher abundance than its comigration with KIF3A/B/KAP3 (Fig. 3 E, bottom panel). Given that KIF3A/B/KAP3 primarily elutes in a molecular weight range suggestive of a cargo-free state, the comigrating TRIM46 signal in this fraction likely reflects its self-assembled dimeric/trimeric states instead of a stable association with the KIF3/KAP3 heterotrimer. Thus, the specific interaction of TRIM46 with KIF3B/B/KAP3, but not with KIF3A/B/KAP3, supports the idea that alternative KIF3 assemblies may contribute to cargo selectivity. Although KIF3A/B/KAP3 is more abundant, the minor KIF3B/B/KAP3 fraction fulfills a distinct role by targeting TRIM46, highlighting specialization among kinesin-2 assemblies.

The KIF3B/B/KAP3 can be reconstructed stably in addition to the KIF3A/B/KAP3

To test the potential discrepancy among dimeric KIF3 subtypes resulting from the C-terminal difference, recombinant proteins of C-terminal domains of KIF3A (AC, 376-701; ACT, 481-701; AT, 600-701) and 3B (BCT, 475-741; BT, 592-701) were constructed and purified for biochemical assessments (Fig. 4 A). Pull-down results indicated that both tail regions of KIF3A and 3B could bind KAP3 independently, and the coiled-coil region was required to form heterotrimeric KIF3A/B/KAP3 (Fig. 4 B). To eliminate potential GST-induced oligomerization, we next repurified all possible KIF3 complexes by replacing GST-tagged KIF3A with His-tagged constructs and assessed them using analytical SEC (Fig. 4 C). Most likely, as a result of the stronger and longer coiled-coil region possessed by KIF3A relative to 3B (Fig. S2 B) that arises from differences in their amino acid sequences (Fig. S2 C), KIF3A/A (ACT-ACT, AA) and KIF3A/B (ACT-BCT, AB) exhibited high–molecular weight states in solution, while KIF3B/B (BCT-BCT, BB) displayed a stable dimer state (Fig. 4 C). Interestingly, when the adaptor protein KAP3 was premixed, AB was stabilized by forming a heterotrimeric complex AB-KAP3 (ABK) with an elution volume similar to BB–KAP3 (BBK), but the AA–KAP3 (AAK) complex remained as high–molecular weight species (Fig. 4 C). The above biochemical results suggested the potential existence of both the KIF3A/B/KAP3 and KIF3B/B/KAP3 complexes. Collectively, the above biochemical and cellular findings indicated the coexistence of multiple KIF3/KAP3 assembly states, including KIF3A/B/KAP3 and KIF3B/B/KAP3, as well as KIF3B dimers in the absence of KAP3.

While the use of truncated constructs represents a limitation, our biochemical data show that KIF3B dimers can form a stable KIF3B/B/KAP3 complex in vitro. This supports the potential physiological relevance of this alternative complex and suggests that multiple KIF3/KAP3 stoichiometries coexist endogenously.

KIF3B/B/KAP3 exhibits a C-terminal structure distinct from KIF3A/B/KAP3

KIF3A/B/KAP3 transports vesicles containing membrane proteins such as NMDA receptors and N-cadherin via APC (Ichinose et al., 2015; Alsabban et al., 2020). The formation of high–molecular weight assemblies of KIF3A-containing complexes, as observed by SEC, likely facilitates the recruitment of multiple motors to a single-cargo membrane, enabling cooperative transport of high-load cargo for stable, long-distance movement within neurons (Schimert et al., 2019; Jiang et al., 2025a). In contrast, our experiments indicate that KIF3B/B/KAP3 primarily transports TRIM46, a cytoplasmic protein involved in MT bundling at the AIS. Since TRIM46 functions in a cytosolic context, a 1:1 interaction between KIF3B/B/KAP3 and TRIM46 may be sufficient, without requiring the formation of high–molecular weight assemblies. To further elucidate these transport mechanisms, it is crucial to confirm whether KIF3A/B/KAP3 and KIF3B/B/KAP3 recognize distinct cargos via their respective tail domains. Our previous work has already provided SAXS-based structural insights into the KIF3A/B/KAP3 complex (Jiang et al., 2023). Thus, we next sought to understand the biochemical and structural bases underlying the potential cargo-binding ability and specificity of KIF3B/B/KAP3. The highly purified BBK proteins (Fig. 5 A, left panel) were assessed by the combination of SEC and multiangle light scattering (MALS) (SEC-MALS) analysis. As a result, the molecular weight of the BBK complex was determined to be 141 kDa, corresponding to a 2:1 stoichiometric ratio (Fig. 5 A, right panel).

The BBK proteins were further examined by SEC-SAXS analysis, and the frame region with the steady radius of gyration (Rg) shown in the chromatogram was selected for data analysis (Fig. 5 B). As a result, the real-space Rg and Dmax were estimated to be ~62.5 and 280 Å for BBK (Fig. 5 C; and Fig. S2, D–E). The final averaged SAXS model of BBK showed an elongated profile (Fig. 5 A) similar to the previous reported ABK model (Jiang et al.,

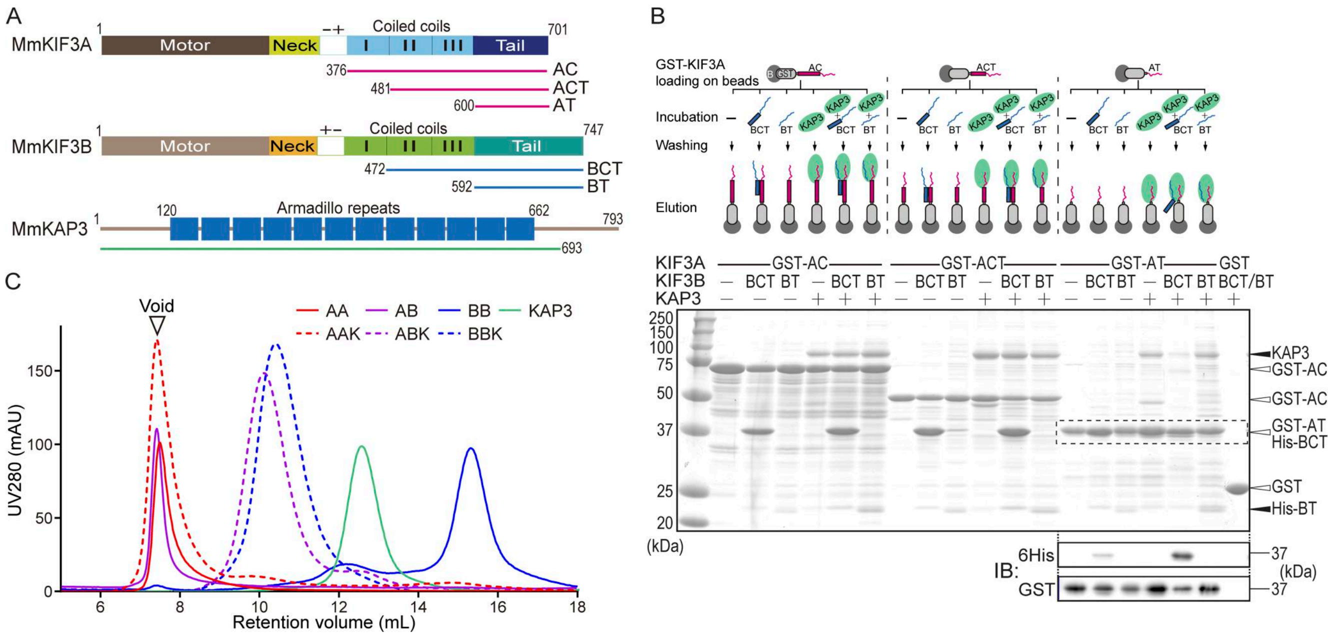

Figure 4. **Biochemical analyses indicated the existence of different KIF3/KAP3 subtypes in vitro.** **(A)** Schematic diagrams showing the major constructs used for biochemical analysis, which are tagged by 6×His or GST for different uses. AC, KIF3A 376–706, CC1–CC2–CC3-tail construct; ACT, KIF3A 481–701, CC2–CC3-tail construct; AT, KIF3A 600–701, tail construct; BCT, KIF3B 475–747, CC2–CC3-tail construct; BT, KIF3B 592–747, tail construct. **(B)** Pull-down assay evaluating the interaction among KIF3A, KIF3B, and KAP3. In the GST-AT group, because His-BCT and GST-AT have similar molecular weights, western blotting was probed with anti-6×His and anti-GST antibodies. The observation that GST-ACT and His-BCT are present at equal levels in lane eight suggests the formation of a dimer. The comparable levels of His-BT (20 kDa) in lanes 12 and 18 are consistent with an indirect interaction between KIF3A and KIF3B mediated by KAP3 (AT–KAP3–BT) and further suggest that direct AB dimer formation requires the coiled-coil region. Note that KAP3 band intensities are equivalent after normalization to the GST immunoblot signal in lanes 16–18. B, beads of glutathione agarose. **(C)** Analytical SEC analysis of reconstructed KIF3 and KIF3/KAP3 complexes. His-tagged KIF3A constructs were used for all the complex purification. AAK: ACT/ACT/KAP3. Source data are available for this figure: SourceData F4.

2023), but significant discrepancies between ABK and BBK were observed in the scattering curves and real-space $P(r)$ distance distribution (Fig. S2, D–E; and Table S1), indicating the difference between their conformations. ABK exhibits several laterally bulging surfaces, while BBK is flat in lateral view but shows significant swelling in the lower part (Fig. 5, D–E). Remarkably, the KIF3 tail-KAP3 regions (excluding the elongated coiled-coil segment) of ABK and BBK showed distinct shapes of the potential cargo-binding cavity (Fig. 5 F).

These structural findings suggest that KIF3A/B/KAP3 and KIF3B/B/KAP3 have distinct cargo-binding conformations that likely underlie their cargo specificity. Complexes capable of forming high–molecular weight assemblies, such as KIF3A/B/KAP3, may be optimized for long-distance vesicle transport, whereas complexes that do not form such assemblies, including KIF3B/B/KAP3, may preferentially mediate short-range cytosolic transport. Notably, analyses of the mammalian KIF3 motor domains by the Gilbert group revealed that homo- and heterodimeric KIF3 motors exhibit distinct ATPase catalytic properties and run lengths (Albracht et al., 2014; Guzik-Lendrum et al., 2015; Deeb et al., 2019) and that heterodimerization alters entry into a processive run along MTs without affecting stepping within the run (Quinn et al., 2018). These differences in the motor properties of KIF3A/B/KAP3 and KIF3B/B/KAP3 further support their functional adaptation to transport over different distances.

Early studies across multiple organisms established the prevailing view that kinesin-2 functions predominantly as a heterotrimeric complex (Cole et al., 1993; Cole et al., 1998; Vernos et al., 1993; Waither et al., 1994; Pesavento et al., 1994; Yamazaki et al., 1995, 1996; Wedaman et al., 1996; Signor et al., 1999). However, whether alternative dimeric forms contribute to physiological specificity has remained largely unexplored, particularly in mammalian neurons where kinesin-2 motors act beyond cilia. More recent work by Garbouchian et al. (2022) provided important insights by demonstrating that KAP serves as an adaptor for both KIF3A/B and KIF3A/C in mammalian neurons (Garbouchian et al., 2022); however, because this study relied on overexpression, it did not address the composition of endogenous complexes. Our study provides evidence that, in addition to the canonical KIF3A/B/KAP3 complex, mammalian neurons contain heterogeneous KIF3/KAP3 assemblies, including a KIF3B-enriched, KAP3-associated population with distinct cargo preferences. TRIM46 interacts with KIF3B/B/KAP3 but not with KIF3A/B/KAP3, suggesting that homodimeric KIF3B motors may play a specialized role in axonal development that cannot be substituted by heterodimeric KIF3A/B (Fig. 5 G).

These findings help to reconcile why KIF3B-enriched assemblies were overlooked in earlier studies. Most prior work relied on ciliary systems, whole-animal mutants, or overexpression-based assays, experimental contexts not ideally suited for detecting endogenous diversity of KIF3 assemblies. By combining

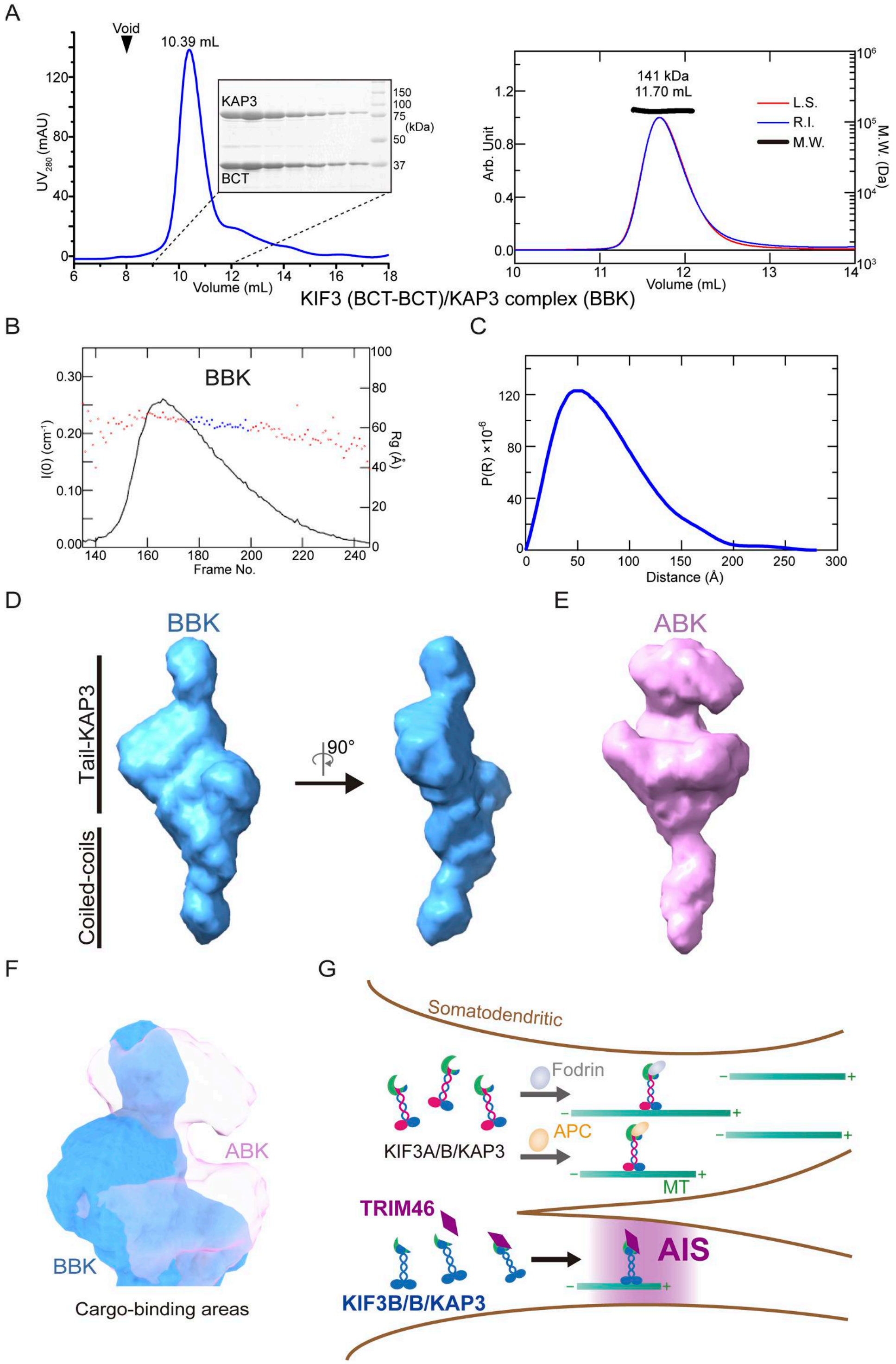

Figure 5. **KIF3B/B/KAP3 has a unique C-terminal structure underlying its cargo specificity. (A)** Reconstruction and biochemical evaluation of KIF3/KAP3 BBK complex. Analytic SEC assay and SDS-PAGE result of purified BBK (KIF3-BCT/BCT/KAP3) complex (left panel); SEC-MALS analysis of the BBK complex (right panel). The MW of the complex was found to be 141 kDa, which is close to the theoretical calculation with a 2:1 binding ratio. **(B)** R_g and *I(0)* versus number of diffraction frames from SEC-SAXS experiment measuring the BBK. **(C)** Pair distribution function P(r) of the BBK. **(D)** SAXS-based structural outline of BBK. **(E)** SAXS model of ABK (SASBDB ID: SASDMV5). **(F)** Superposition of the tail-KAP3 region (excluding the elongated coiled-coil segment) of BBK with ABK. **(G)** Model depicting specific cargo transport by various KIF3/KAP3 subtypes for distinct functions. Source data are available for this figure: SourceData F5.

high-resolution microscopy with rigor-state extractions, we detected KIF3B-only puncta in axons under specific developmental stages, consistent with our prior observation that TRIM46 transport is activated at DIV4, a critical stage for AIS formation (Ichinose et al., 2019). Together with evidence from Caenorhabditis *elegans* showing that certain kinesin-2 homodimers retain processivity (Brunnbauer et al., 2010), our results suggest that compositional flexibility is an inherent feature of kinesin-2, enabling redundancy or specialization depending on cellular context.

Functionally, the compositional variety of KIF3/KAP3 complexes likely contributes to cargo specificity and spatial regulation of transport. Structural differences between KIF3A/B/KAP3 and KIF3B/B/KAP3 may determine distinct modes of cargo binding, potentially influenced by posttranslational regulation such as phosphorylation (Ichinose et al., 2015; Ichinose et al., 2019). Moreover, motor coordination is expected to be critical: kinesin complexes capable of forming high–molecular weight assemblies, such as KIF3A-containing complexes, may be optimized for long-distance, high-load transport by recruiting multiple motors, whereas complexes that do not form such assemblies, such as KIF3B/B/KAP3, may specialize in short-range delivery within the proximal axon. This model aligns with cargo preferences observed in neurons, where KIF3A/B transports synaptic proteins over long distances (Ichinose et al., 2015; Alsabban et al., 2020), whereas KIF3B/B primarily delivers TRIM46 to the AIS (Ichinose et al., 2019). Notably, the modes of interaction between KIF3 and different TRIM family proteins are not fully conserved. For example, biochemical analyses of the testis-specific TRIM60 indicate that it binds KIF3A/B in a KAP3-independent manner (Huang et al., 2012). In contrast, our results demonstrate that binding to the neuronal TRIM46 requires KAP3 but is independent of KIF3A (Fig. 3 A), likely reflecting fundamental differences in the structural and functional organization of these TRIM proteins.

Looking forward, our findings regarding KIF3B-enriched assembles expands the compositional and functional diversity of kinesin-2 motors, highlighting new avenues for investigation. Future studies should clarify the structural basis of cargo binding by combining high-resolution structural approaches, such as cryo-EM or NMR, with functional assays of transport specificity. Computational predictions may provide additional insights, though their current reliability for these flexible tail–adaptor complexes remains limited. Emerging evidence that intrinsically disordered motor protein tails can adopt regulated structures calls for a re-examination of transport selectivity (Niu et al., 2026). Understanding these mechanisms will not only elucidate how neurons achieve precise spatiotemporal protein distribution but may also reveal general principles of motor protein adaptability across diverse cellular contexts.

Materials and methods

Cell culture

Neuro2a cells (RCB Cat# RCB2639, RRID:CVCL_0470) were obtained from the RIKEN Cell Bank. It was deposited at RIKEN by Hiroshi Fukuda. The animal species was verified by detecting mitochondrial DNA sequences (Fw: 5′-GCACTGAAAATGCTTAGATGGATAATTG-3′, Rv: 5′-CCTCTCATAAACGGATGTCTAG-3′; reference sequence: GenBank NC_005089). The cells were introduced to Gunma University after authentication (Lot #3). Neuro2a cells were cultured in High-Glucose DMEM (FUJIFILM Wako) supplemented with 10% fetal bovine serum (Biowest) in T75 flasks (Thermo Fisher Scientific) at not >80% confluency. Hippocampi were dissected from ICR mice (Charles River; IMSR Cat# CRL:022, RRID:IMSR_CRL:022) on embryonic day 16. No gender determination was done, and three or more embryos were used. The hippocampi were digested with 0.25% trypsin (Thermo Fisher Scientific) in HBSS (FUJIFILM Wako) for 15 min at 37°C. Dissociated hippocampal cells were seeded at a density of 3 × 10^4 cells per well on 8-well chamber covers (Matsunami Glass) coated with 0.04% polyethylenimine (Merck) and BioCoat poly-D-lysine (Corning). All primary neurons were cultured in MEM (Thermo Fisher Scientific) supplemented with 1 mM pyruvate (Thermo Fisher Scientific), 0.6% glucose, 2 mM GlutaMAX (Thermo Fisher Scientific), 2% B27 Plus (Thermo Fisher Scientific), and 100 U/ml Penicillin-Streptomycin (Thermo Fisher Scientific). The cells were maintained at 37°C in a humidified atmosphere of 95% air and 5% CO_2. These experiments have passed a rigorous ethical review and have been approved by Gunma University for animal experiments (approval number: DO23-076) and genetic recombination experiments (approval number: 23-076).

Vector construction for imaging and transfection

KIF3A was amplified from a RIKEN cDNA library (AK169425) using the primers 5′-GCGGAATTCTATGCCGATCAATAAGTCGGAGAAG-3′ or 5′-GCCCTCGAGCCACCATGTACCCATACGATGTTCCAGATTACGCTATGCCGATCAATAAGTCGGAGAAG-3′, together with 5′-GCGGGATCCTTACTGAAGTAAAGAATCAATTACGG-3′. The amplified fragments were inserted into EGFP-C1 via the EcoRI-BamHI sites or into pcDNA3.1(−) via the XhoI-BamHI sites, generating EGFP-KIF3A and HA-KIF3A constructs, respectively. KIF3B was amplified from a RIKEN cDNA library (AK147467) using the primers 5′-GCGGCTAGCGCCACCATGGAGCAGAAACTCATCTCTGAAGAGGATCTGATGTCCAAGTTAAAAAGCTCAG-3′ and 5′-GCGCTCGAGTTAATGGTGGTGATGGTGATGATGCTTGGGAACCAGCCCC-3′ and cloned into pcDNA3.1(−) via the NheI-XhoI sites, generating a myc-KIF3B-His7 construct. TRIM46 and TRIM46 ΔRING were amplified from TRIM46-TagRFP (XM_006501614; Ichinose et al., 2019) using the primers 5′-GCCGAATTCGCCACCATGGGTGGTGCCCTTGAA-3′ or 5′-GCCGAATTCGCCACCATGGTGAGTGTGGGAGGAGCC-3′, together with 5′-GCCGTCGACTGGTCCAGTTTGGCAAAGCCC-3′. The PCR products were inserted into EGFP-N1 via the EcoRI-SalI sites.

The shRNA target sequence was designed for protein KD using the RNAi Designer tool (VectorBuilder). A cassette containing the pre-shRNA sequence was inserted into pBAsi-mU6 (Takara Bio). The target sequences of each shRNA are as follows: Negative control, 5′-GCCTAAGGTTAAGTCGCC-3′; KIF3A #1, 5′-GGCCTGATGTGGGAGTATATA-3′; KIF3A #2, 5′-ATATTGGGCCAGCAGATTATA-3′; KIF3A #3, 5′-GCAAAGCCTGAGACCGTAATT-3′; KIF3A #4, 5′-GCCTGAGACCGTAATTGATTC-3′; KIF3B #1, 5′-GCTCAAAGAGAGACCAGATAC-3′. For volume marker, EGFP was amplified from the EGFP-N1 vector using CMV primer (5′-CGCAAATGGGCGGTAGGCGTG-3′) and 5′-GCGAATTCTTGCCGATTTCGGCCTATTGG-3′, digested with XhoI and EcoRI, and subsequently inserted into the XhoI-MfeI sites of pBAsi-mU6-Neo. Oligonucleotides were synthesized (Integrated DNA Technologies, Inc.) to assemble an insertion cassette for cloning into the BamHI-HindIII sites. The 5′-CTCGAG-3′ (XhoI) sequence was included as a spacer to facilitate proper hairpin formation and efficient transcription from the U6 promoter. Two complementary oligonucleotides, 5′-GATCC-3′-(target sequence)-5′-CTCGAG-3′-(antisense target sequence)-5′-TTTTTGA-3′ and 5′-AGCTTCAAAAA-3′-(target sequence)-5′-CTCGAG-3′-(antisense target sequence)-G, were annealed and inserted into the pBAsi-mU6-EGFP vector.

CRISPR/Cas9-mediated gene editing was performed using the pORANGE vector as the backbone (Willems et al., 2020). In the control condition, no gRNA sequence was inserted. The KIF3B KO construct was designed using CRISPick (https://portals.broadinstitute.org/gppx/crispick/public), with the gRNA sequence being 5′-GCACAGAGTCCACGAGTGGT-3′. The design introduced an insertion of 5′-GAATTCTTAA-3′, resulting in a stop codon after proline at position 79 in the motor domain. Annealed oligonucleotides 5′-CACCGCACAGAGTCCACGAGTGGT-3′ and 5′-AAACACCACTCGTGGACTCTGTGC-3′ were inserted into the BbsI site of pORANGE. In addition, annealed oligonucleotides 5′-AGCTGCACAGAGTCCACGAGTGGTCGGGAATTCTTAAGCACAGAGTCCACGAGTGGTCGG-3′ and 5′-GATCCCGACCACTCGTGGACTCTGTGCTTAAGAATTCCCGACCACTCGTGGACTCTGTGC-3′ were inserted into the HindIII-BamHI sites. For the resistant KIF3B construct, a silent mutation (from 5′-TTCCGACCACTCGTG-3′ to 5′-TTTAGGCCCTTAGTC-3′) was introduced into the region corresponding to amino acids 77–81 (FRPLV) by overlap PCR and cloned into pcDNA3.1(−). Using the CMV primer (5′-CGCAAATGGGCGGTAGGCGTG-3′), 5′-GAACTCGAGGTTACTTGGGAACCAGCCC-3′, and the overlap primers 5′-CGTTTAGGCCCTTAGTCGACTCTGTGCTGCAGGGTTTC-3′ and 5′-CGACTAAGGGCCTAAACGTCTCATCATAGAGCTCAA-3′, the fragment was amplified from myc-KIF3B-His7 and inserted into pcDNA3.1(−) via the NheI-XhoI sites, generating a myc-KIF3B construct lacking the C-terminal His7 tag.

Transfection of Neuro2a cells was performed using Lipofectamine 3000 (Thermo Fisher Scientific) according to the manufacturer's instructions. Gene delivery into primary cultured hippocampal neurons is described in subsequent sections.

Electroporation

Electroporation was performed using the Neon Transfection System (Thermo Fisher Scientific). Dissociated neurons were spun down at 100 × g for 5 min and resuspended in R buffer (Thermo Fisher Scientific) at a concentration of 6×10^6 cells/ml. 11 µl of the resuspended solution was mixed with 1 µg of DNA. For KIF3A KD, an equal amount of four types of KD vectors was combined, and 1 µg of the mixture was used. For other experiments, a single type of vector was used. The mixed solution was aspirated into a 10 µl Neon Tip and subjected to electroporation under the following conditions: pulse voltage = 1,400 V, pulse width = 20 ms, and pulse number = 1. After electroporation, all neurons were seeded into one well of an 8-well chamber.

Immunostaining

Cells were initially washed with PBS at 37°C and then fixed with 4% paraformaldehyde for 20 min. Next, they were permeabilized with 0.1% Triton X-100 for 3 min and blocked with 5% BSA (Merck) in PBS for 20 min. Primary antibodies, diluted in Can Get Signal Solution (Toyobo), were incubated with the cells for 16–18 h at 4°C. This was followed by incubation with secondary antibodies for 1 h at room temperature. For sequential staining, the first primary and secondary antibody incubation were performed under the same conditions described above, after which the cells were fixed again with 4% paraformaldehyde for 10 min before incubation with the second set of antibodies under identical conditions.

The primary antibodies and concentrations used in this study are as follows: Mouse anti-KIF3A (Cat# 611508; BD Biosciences, RRID:AB_398968, 1:200), rabbit anti-KIF3B (Cat# KIF3B; N. Hirokawa—University of Tokyo, Tokyo, Japan, RRID:AB_2715472, 1:2,000), mouse anti-KAP3 (Cat# 610637; BD Biosciences, RRID:AB_397967, 1:500), guinea pig anti-AnkG (Cat# MSFR107220; Nittobo Medical, 1:1,000), rabbit anti-TRIM46 (Cat# 21026-1-AP; Proteintech, RRID:AB_10732843, 1:4,000), mouse anti-HA (Cat# 2367; Cell Signaling Technology, RRID:AB_10691311, 1:1,000), rabbit anti-HA (Cat# 3724; Cell Signaling Technology, RRID:AB_1549585, 1:1,000), chicken anti-MAP2 (Cat# NB300-213; Novus, RRID:AB_2138178, 1:5,000), rabbit anti-myc (Cat# 562S; MBL International, RRID:AB_591114, 1:1,000), mouse anti-myc (Cat# 2276; Cell Signaling Technology, RRID:AB_331783, 1:1,000), and mouse anti-α-tubulin (Cat# T9026; Sigma-Aldrich, RRID:AB_477593, 1:5,000).

The secondary antibodies and concentrations used in this study are as follows: Donkey anti mouse IgG (H+L) Alexa Fluor 405 (Cat# ab175658; Abcam, RRID:AB_2687445, 1:1,000), donkey anti mouse IgG (H+L) Alexa Fluor 488 (Cat# 715-546-151; Jackson ImmunoResearch Labs, RRID:AB_2340850, 1:1,000), donkey anti guinea pig IgG (H+L) Alexa Fluor 488 (Cat# 706-546-148; Jackson ImmunoResearch Labs, RRID:AB_2340473, 1:1,000), donkey anti rabbit IgG(H+L) CF568 (Cat# 20098-1; Biotium, RRID:AB_10853318, 1:4,000), donkey anti mouse IgG (H+L) CF633 (Cat# 20124-1; Biotium, RRID:AB_10853607, 1:2,000), and Donkey anti Chicken IgY (IgG) (H+L) Alexa Fluor 647 (Cat# 703-605-155, RRID:AB_2340379, 1:1,000). In cases where the primary antibodies were raised in the same host species, labeling was performed using the FlexAble Antibody Labeling Kit (Proteintech) according to the manufacturer's protocol.

Imaging

All imaging was performed using a Zeiss LSM 880 confocal laser-scanning microscope equipped with a 63×/1.4 NA Plan-Apochromat oil DIC M27 objective (Zeiss). Imaging was conducted at room temperature, with a measured temperature of 26 ± 2°C. Fixed cells were imaged in PBS, and no oxygen scavenger system was used. Fluorophores were as described for each secondary antibody and were detected sequentially, one channel at a time from longer to shorter wavelengths, using GaAsP-PMT detectors with 405-, 488-, 561-, and 633-nm laser lines. For high-resolution imaging (Fig. 2 A, and D; and Fig. S1, C and N), images were acquired with a 3× scan zoom and a pixel dwell time of 8.24 µs. All other images were acquired with a 1× scan zoom and a pixel dwell time of 4.12 µs. Images were acquired at a resolution of 1,024 × 1,024 pixels and were cropped as necessary. Image acquisition was performed using the microscope-associated ZEN software (Zeiss). For observations used in nearest-centroid distance measurements (Fig. 2 A), post-acquisition deblurring was applied in ZEN with the following parameters: strength = 0.9, blur radius = 15, and sharpness = 0.0. For figure presentation, brightness was adjusted uniformly within each experiment by modifying only the maximum intensity value, while the γ value was fixed at 1.

Image analysis

For KD and KO experiments, images were acquired with the same condition throughout the experiments. For quantification of KIF3, cell bodies were manually selected, and the average intensity of signals was measured using the measurement function in FIJI (Schindelin et al., 2012). For quantification of TRIM46, the most proximal part of the longest neurites was selected manually using a 10-pixel-wide segmented line based on the EGFP channel for KD experiment or MAP2 channel for KO experiment (Fig. S1 I), and the intensity of TRIM46 was measured using the Plot Profile function in FIJI. A one-dimensional Gaussian filter with a sigma of six was applied to the raw data. The first continuous length where the intensity exceeded 1,000 AU was defined as the TRIM46 accumulation length. This length was recorded for each image and used for statistical analysis.

For enrichment analysis, a binary mask corresponding to the top 5% of HA signal intensity was generated for each image. KIF3 enrichment was defined as the ratio of mean KIF3 intensity within the HA-high mask to that in the complementary HA-low region. To estimate chance-level enrichment, the HA-high mask was randomly shifted in the x and y directions (30–50 pixels; 25 iterations), and the mean enrichment across these shifts was used as a control.

For KIF3 component co-localization experiments, images were acquired under identical conditions with 3× optical zoom. For each protein combination, the proximal 25–40 µm of the longest neurite was imaged. After acquisition, images were deblurred using ZEN (ZEISS) and processed in Fiji with a custom macro: files were split into channels, thresholded (C1: 5000–65535; C2: 6000–65535; 16-bit units, black background enabled), converted to binary masks, and segmented using Watershed. Puncta >10 pixels were identified using Analyze Particles, and centroid coordinates were extracted. The minimum Euclidean distance was calculated by determining the distance from each punctum's centroid to all centroids of the other puncta using Python, and the minimum value was identified. To avoid biasing the statistical analysis, 10 minimum distances per image were randomly sampled using Python. Statistical tests were performed using the methods described in the figure legends.

Saponin permeabilization to visualize MT-bound kinesin

To visualize rigor-state MT-bound kinesin, primary cultured neurons were transfected using the calcium-phosphate precipitation method (Ichinose et al., 2023). Briefly, on DIV4, 0.9 µg each of EGFP-KIF3A and myc-KIF3B was mixed with 3.1 µl of 2 M $CaCl_2$ and brought to a final volume of 25 µl with H_2O. The mixture was added in one-eighth aliquots to 25 µl of 2× HBS, followed by 10 rounds of pipetting and 2 s of vortexing, repeated eight times, and then incubated for 15 min to allow formation of Ca-DNA precipitates. Neurons were first exchanged into 250 µl of fresh culture medium, after which 12 µl of the Ca-DNA suspension per well was added. Cells were incubated in a 5% CO_2 incubator for 40 min to allow uptake of Ca-DNA particles. The medium was then replaced with fresh medium pre-equilibrated in a 10% CO_2 incubator for 15 min to solubilize excess Ca-DNA particles, after which cells were returned to the original culture medium. Cells were permeabilized 8 h after transfection to minimize aggregation resulting from protein overexpression. The permeabilization procedure was modified from previously established methods (Nakata and Hirokawa, 1995; Ichinose et al., 2015) as described below to minimize damage to immature neurons.

Neurons were washed with 37°C BRB80 buffer (80 mM PIPES, 1 mM MgCl2, and 1 mM EGTA, pH 6.8) and permeabilized with extraction buffer, BRB80 containing 50 µM ATPγS (FUJIFILM WAKO), 0.05% saponin, and 10 µM paclitaxel (FUJIFILM WAKO) for 1 min at 37°C to allow overexpressed cytosolic proteins to diffuse out. Samples were then washed with extraction buffer without saponin for 2 min and fixed in 4% PFA/BRB80 for 20 min. Immunostaining was performed following standard procedures after fixation. For co-localization analysis of KIF3A and KIF3B, a 10-µm segment at the proximal region of axons or somatodendritic compartments was selected. ROIs were defined based on the α-tubulin staining, and Pearson's correlation coefficients were calculated using the Coloc2 plugin in FIJI.

CHX chase assay

Neuro2a cells were transfected with myc-KIF3B-His7 together with TRIM46-EGFP wild-type or ΔRING constructs (Ichinose et al., 2019) using Lipofectamine 3000 (Thermo Fisher Scientific) according to the manufacturer's instructions. Twenty-four hours after transfection, cells were treated with CHX (FUJIFILM WAKO) at a final concentration of 50 µg/ml. Cells were harvested at 0, 0.5, 1, 2, 4, and 6 h after CHX addition. For each time point, culture dishes (60 mm) were washed once with ice-cold PBS and lysed directly on plates in ice-cold RIPA buffer (50 mM Tris-HCl, pH 7.4, 150 mM NaCl, 1% NP-40, 0.1% SDS, and 0.5% sodium deoxycholate) supplemented with cOmplete ULTRA mini EDTA-free protease inhibitors (MERCK). Lysates were clarified by centrifugation (15,000 × *g*, 10 min, 4°C). Supernatants were mixed with 4× Laemmli buffer containing β-mercaptoethanol, boiled for 5 min, and subjected to SDS-PAGE.

Proteins were transferred to polyvinylidene difluoride (PVDF) membranes (Immobilon 0.2 µm; MERCK). Membranes were blocked with 5% skim milk in TBS-T (50 mM Tris-HCl, pH 7.5, 150 mM NaCl, and 0.1% Tween-20) for 1 h at room temperature. Immunoblotting was performed with rabbit anti-myc (Cat# 562S; MBL International, RRID:AB_591114, 1:1,000) to detect KIF3B, rabbit anti-GAPDH (Cat# 2118; Cell Signaling Technology, RRID:AB_561053, 1:1,000) as a housekeeping control and rabbit anti-GFP (Cat# 598S; MBL International, RRID:AB_591816, 1:1,000), followed by HRP-conjugated secondary antibody donkey anti-rabbit IgG (Cat# 711-036-152; Jackson ImmunoResearch Labs, RRID:AB_2340590, 1:20,000). Signals were visualized by ImmunoStarR Zeta (FUJIFILM WAKO) and captured with a

LAS4000 (Cytiva). Band intensities were quantified using ImageQuantTL (Cytiva). Intensities were expressed relative to the t = 0-h sample (set to 1.0).

For quantification, lanes were manually defined according to the instructions provided in the ImageQuant TL software, after which background and band intensities were automatically measured. The resulting data were exported as CSV files, and statistical analyses were performed using Microsoft Excel or Python. The same quantification procedure was applied to all subsequent immunoblotting analyses.

Ubiquitination assay

Neuro2a cells were transfected with myc-KIF3B-His7 together with TRIM46-EGFP wild-type or ΔRING constructs using Lipofectamine 3000. Twenty-four hours after transfection, cells in culture dishes (12 cm) were lysed with denaturing buffer consisting of 6 M guanidine-HCl, 100 mM NaH_2PO_4, and 10 mM Tris-HCl (pH 8.0). Lysates were cleared by centrifugation (15,000 × *g*, 10 min, 4°C) and incubated with 50 µl of TALON resin (Takara Bio) for 1 h at 4°C with gentle rotation. After binding, beads were washed with 20 volumes of denaturing buffer containing 20 mM imidazole three times and subsequently washed with 20 volumes of TBS.

Bound proteins were eluted directly in 2× Laemmli sample buffer containing 250 mM imidazole and β-mercaptoethanol by boiling at 95°C for 5 min. Eluates and input fractions diluted with 20 volumes of TBS were subjected to SDS-PAGE and transferred to PVDF membranes. Membranes were blocked with 5% BSA in TBS-T and probed with anti-ubiquitin (Cat# U5379; Sigma-Aldrich, RRID:AB_477667, 1:100), followed by HRP-conjugated secondary antibody donkey anti-rabbit IgG (Jackson ImmunoResearch, 1:20,000). For normalization, membranes were probed with anti-myc (MBL International, 1:1,000) to confirm equivalent recovery of myc-KIF3B-His7.

Band intensities of ubiquitinated molecules migrating above myc-KIF3B-His7 (i.e., >100 kDa) were quantified using ImageQuantTL. Ubiquitin signals were normalized to the amount of recovered myc-KIF3B-His7 (anti-myc) and compared between TRIM46 wild-type and ΔRING conditions.

Constructs, protein expression, and purification

The gene encoding the C-terminal region of *Mus musculus* KIF3A (NCBI accession NP_032469.2; residues 481–701, ACT) was cloned into the pETDuet-1 vector with an N-terminal 6×His tag. The C-terminal region of *M. musculus* KIF3B (NCBI accession NP_032470.3; residues 475–747, BCT) was cloned into the second multiple cloning site of the same vector without an affinity tag to enable co-expression of the KIF3A/B tail heterodimer. For pull-down assays, the same sequences were subcloned into the pGEX-6p-3 vector to generate N-terminal GST fusion proteins. In addition, truncated constructs of KIF3A (AC, residues 376–701; AT, residues 600–701) and KIF3B (BT, residues 592–747) were generated by PCR and cloned into the pGEX-6p-3 or pETDuet-1 vectors as indicated. The *M. musculus* KAP3A (residues 1–693; NCBI accession NP_001292572.1) was PCR amplified and cloned into the pET-21b vector without affinity tags. Recombinant plasmids were transformed into *Escherichia coli* BL21 (DE3) cells (Novagen). Protein expression was induced with 0.5 mM isopropyl β-D-1-thiogalactopyranoside at 16°C for 20 h. Cells were harvested, lysed by sonication, and clarified by centrifugation at 16,000 × *g* for 30 min. The supernatant was subjected to Ni–NTA affinity chromatography in buffer containing 20 mM Tris-HCl (pH 8.0), 300 mM NaCl, 5% glycerol, and protease inhibitors. Proteins were eluted with imidazole and further purified by SEC using a Superdex Increase 200 column (GE Healthcare) equilibrated in buffer containing 20 mM HEPES (pH 8.0), 150 mM NaCl, and 1 mM DTT. Purified proteins were concentrated to ~10 mg/ml by ultrafiltration, flash-frozen in liquid nitrogen, and stored at −80°C.

IP and pull-down assays

Mouse brain tissues were homogenized in cold homogenization buffer. The homogenate was first centrifuged at 1,000 × *g* to remove cell debris and nuclei (P1). The resulting supernatant (S1) was further centrifuged at 12,000 × *g* to obtain the P2 pellet (crude synaptosomes and mitochondria) and the S2 supernatant fraction (light membranes and cytosolic proteins). The S2 fraction was then subjected to ultracentrifugation at 100,000 × *g* for 1 h to separate the microsome-enriched pellet (P3) from the final S3 fraction, which contains only the soluble cytosolic proteins.

IP of brain lysate was performed following established protocols (Ichinose et al., 2019). The precleaned brain S2 fractions were incubated with Protein A-Sepharose (Cytiva) beads containing rabbit polyclonal anti-KIF3B (RRID:AB_2715472), rabbit polyclonal anti-TRIM46 (RRID:AB_10732843), or rabbit normal IgG antibodies (RRID:AB_2334717) for 3 h at 4°C in buffer containing 50 mM Tris-HCl, pH 8.0, 150 mM NaCl, 0.01% CHAPS, 0.1% Triton X-100, and protease and phosphatase inhibitors. The protein complex was eluted with boiled sample buffer consisting of 125 mM Tris-HCl (pH 6.8), 4% SDS, 20% glycerol, and 0.01% BPB and then analyzed using SDS-PAGE and western blotting.

For the pull-down analysis of binding within KIF3A/B/KAP3 complex, *E. coli* cells expressing the bait proteins (GST-fusion C-terminal KIF3A or 3B truncations) (Fig. 4 B) were premixed with each group of the cells containing overdosed input proteins and lysed by sonication with a buffer of 20 mM Tris-HCl, pH 8.0, 150 mM NaCl, 7 mM β-ME, and 5% (vol/vol) glycerol. After centrifugation, the supernatants were loaded onto the balanced Glutathione Sepharose 4B beads (Cytiva) and incubated for 30 min on ice; the beads were then washed three times with the buffer to remove unbound proteins. For the pull-down assays probing the cargo binding, mouse brain S2 fractions were further applied to the beads containing each group of KIF3/KAP3 complex and then washed to remove unbound proteins. The bound proteins were finally eluted with 10 mM reduced glutathione, and the eluates were analyzed using SDS-PAGE and western blotting. A control group using GST protein as bait was included.

Immunoblotting

The proteins from the pull-down and IP assays were separated on 10% SDS-PAGE gels for others and transferred to PVDF membranes (Thermo Fisher Scientific); the Brain S3 HiRes-SEC fractions were directly dropped onto the PVDF membranes. The membranes were blocked for 30 min at room temperature with the blocking buffer (3% BSA [m/v] and 0.05% [vol/vol] Tween in TBS). For each specific analysis, the blocked membranes were incubated with the corresponding primary antibody (rabbit polyclonal anti-6×His, 1/1,000, Recenttec; mouse monoclonal anti-GST antibody, 1/2,000, RRID:AB_86554; mouse monoclonal anti-α-fodrin, 1/3,000, RRID:AB_10554860; rabbit polyclonal anti-APC antibody, 1/300, RRID:AB_2057493; mouse monoclonal anti-β-catenin antibody 1/1,000, RRID:AB_397554; rabbit polyclonal anti-TRIM46, 1/1,000, RRID:AB_10732843; mouse monoclonal anti-KIF3A antibody, 1/1,000, RRID:AB_398968; rabbit polyclonal anti-KIF3B, 1/2,000, RRID:AB_2715472; mouse monoclonal anti-KAP3 antibody, 1/1,000, RRID:AB_397967) overnight at 4°C, followed by incubation with the secondary antibodies (anti-mouse/rabbit IgG antibody, 1/5,000, Cytiva) for 30 min at room temperature. Then the membranes were washed and processed with Amersham ECLTM Prime western blotting Detection Reagent (Cytiva) for 2 min, and the signals were detected by chemiluminescence using ImageQuant LAS 4000 (Cytiva).

Analytic SEC assays

For analysis of purified proteins, SEC assays were performed with a Superdex 200 10/300 column (Cytiva) on an Akta Explorer FPLC system (Cytiva) with a SEC buffer (20 mM Tris-HCl, pH 7.5, 150 mM NaCl, and 1 mM DTT). For brain lysate analysis, brain S3 fractions were prepared and assessed by HiRes-SEC with tandem-connected Superdex 200 Increase 10/300 columns (Cytiva), followed by dot blotting analysis. The data were plotted using GraphPad Prism7 (RRID:SCR_002798).

SEC-MALS analysis

MALS was performed in-line with SEC by using an Alliance 2695 high performance liquid chromatography system equipped with Dawn Heleos II 18-angle MALS detectors (Wyatt Technology) and a 2414 Refractive Index (RI) detector (Waters). The obtained data were analyzed by the ASTRA 6.1 software (Wyatt Technology). The data were plotted using GraphPad Prism7.

SEC-SAXS analysis

SEC-SAXS data were collected at beamline BL-10C in Photon Factory (KEK) at 293K using a Prominence-i system (SHIMADZU) coupled to a Superdex 200 Increase 10/300 Gl column (Cytiva). The column was equilibrated with a buffer containing 20 mM Tris-HCl, 200 mM NaCl, 1 mM DTT, and 5% glycerol (pH 8). Serial scattering images were acquired with a 20-s exposure time. Background profiles were generated by averaging 15 images acquired before sample injection. Azimuthal averaging converted the one-dimensional scattering intensity data, which was processed using SAngler (Shimizu et al., 2016). Absolute intensity calibration was based on water as a standard. Scattering profiles from the latter half of elution peaks were used and extrapolated to an infinite dilution condition using MOLASS (Yonezawa et al., 2019; Yonezawa et al., 2023). R_g and forward scattering intensity (I(0)) were calculated via Guinier approximation with AUTORG (Petoukhov et al., 2007), while the pair distribution function (P(r)) was determined using GNOM (Svergun, 1992). Dummy atom models were generated using DAMMIF (Franke and Svergun, 2009) and averaged and selected using DAMAVER (Volkov and Svergun, 2003). Final model calculations were conducted with DAMMIN slow mode starting from the filtered DAMAVER model. The deposition ID in SASBDB is SASDMU5 for BBK (Kikhney et al., 2020). Details of the SEC-SAXS experiment and analysis are summarized in Table S1.

Sequence and structural analysis

Structure-based multiple sequence alignments were performed using the programs Clustal Omega (RRID:SCR_001591). The protein sequences used for analysis were obtained via the NCBI protein database under the accession numbers NP_001287720.1 (*Homo sapiens* KIF3A), NP_001277734.1 (*M. musculus* KIF3A), NP_001093615.1 (*Danio rerio* KIF3A), NP_523934.1 (*Drosophila* Klp64D), NP_497178.1 (*C. elegans* Klp-20), XP_001701510.1 (*Chlamydomonas* FLA10), NP_004789.1 (*H. sapiens* KIF3B), NP_032470.3 (*M. musculus* KIF3B), NP_001093615.1 (*D. rerio* KIF3B), NP_524029.2 (*Drosophila* Klp64D), NP_741473.1 (*C. elegans* Klp-11), and XP_001697037.1 (*Chlamydomonas* FLA8). Structural analysis was performed, and structural figures were generated using the program UCSF ChimeraX (RRID: SCR_015872). The prediction of coiled-coil domains was performed using the DeepCoil (toolkit.tuebingen.mpg.de/tools/deepcoil). The previously reported SAXS result of KIF3 ABK complex (SASBDB ID: SASDMV5) was used for the comparison with BBK (SASBDB ID: SASDMU5) in this study.

Statistics

The statistical methods used are described in the figure legends. Statistical analyses were performed using Microsoft Excel or Visual Studio Code (Microsoft) with Python (Python Software Foundation). Parametric tests were applied under the assumption that the data were normally distributed and exhibited equal variances; however, these assumptions were not formally tested a priori. For comparisons between two groups, two-sided Welch's *t* test was used. For comparisons involving three or more groups, one-way ANOVA was performed, followed by Tukey's post hoc test when a significant effect was detected by ANOVA. The definition of error bars and detailed information on sample size (*n*) and P values are provided in the figure legends, and results of complex post hoc analyses are summarized in Fig. S1 M.

Online supplemental material

Fig. S1 provides comprehensive validation of KIF3A and KIF3B antibodies and genetic perturbations, including shRNA KD and CRISPR-mediated KO in Neuro2a cells and neurons, quantitative analyses of signal reduction and rescue, assessment of antibody epitope specificity and staining order effects, and controls excluding steric interference during AIS co-localization analyses. Fig. S2 presents supporting biophysical, biochemical and sequence analyses of KIF3, including coiled-coil predictions and evolutionary conservation, biochemical fractionation of endogenous complexes, and SAXS characterization comparing the KIF3A/B/KAP3 and KIF3B/B/KAP3 assemblies. Table S1 summarizes SAXS data collection, processing, and model validation statistics for the analyzed KIF3B/B/KAP3 complex.

Data availability

The SEC-SAXS data have been deposited in the SASBDB (https://www.sasbdb.org) under the deposition ID SASDMU5 (https://www.sasbdb.org/project/2454/za79px3zsu/). All other data are provided in the main text and the supplementary information.

Acknowledgments

We thank previous and current members of the NH laboratory for their valuable suggestions and assistance.

This research was supported by Platform Project for Supporting Drug Discovery and Life Science Research (Basis for Supporting Innovative Drug Discovery and Life Science Research) from Japan Agency for Medical Research and Development (AMED) under Grant Number JP21am0101071 (support number 1133), the Japan Society for the Promotion of Science (JSPS) KAKENHI Grant Numbers JP23000013 (N. Hirokawa), JP16H06372 (N. Hirokawa), JP25K09633 (N. Hirokawa), JP19K06516 (N. Shimizu), JP20H05499 (T. Ogawa), JP20K07222 (T. Ogawa), JP24K01519 (T. Ogawa), JP24K09994 (S. Ichinose), JP24K18106 (X. Jiang), JP24KF0141 (X. Jiang), and a research funds supported by JEOL.co.jp (N. Hirokawa) and Eisai.co.jp (N. Hirokawa). X. Jiang acknowledges the support from JSPS as an international research fellow.

Author contributions: Xuguang Jiang: conceptualization, data curation, funding acquisition, investigation, methodology, and writing—original draft, review, and editing. Sotaro Ichinose: data curation, funding acquisition, investigation, methodology, and writing—original draft, review, and editing. Tadayuki Ogawa: conceptualization, data curation, formal analysis, funding acquisition, investigation, methodology, project administration, resources, software, supervision, validation, visualization, and writing—original draft. Kento Yonezawa: investigation. Nobutaka Shimizu: formal analysis, investigation, and resources. Nobutaka Hirokawa: conceptualization, funding acquisition, project administration, supervision, validation, and writing—review and editing.

Disclosures: The authors declare no competing interests exist.

Submitted: 26 March 2025
Revised: 29 September 2025
Accepted: 20 February 2026

References

Albracht, C.D., K.C. Rank, S. Obrzut, I. Rayment, and S.P. Gilbert. 2014. Kinesin-2 KIF3AB exhibits novel ATPase characteristics. *J. Biol. Chem.* 289:27836–27848. https://doi.org/10.1074/jbc.M114.583914

Alsabban, A.H., M. Morikawa, Y. Tanaka, Y. Takei, and N. Hirokawa. 2020. Kinesin Kif3b mutation reduces NMDAR subunit NR 2A trafficking and causes schizophrenia-like phenotypes in mice. *EMBO J.* 39:e101090. https://doi.org/10.15252/embj.2018101090

Bensel, B.M., M.S. Woody, S. Pyrpassopoulos, Y.E. Goldman, S.P. Gilbert, and E.M. Ostap. 2020. The mechanochemistry of the kinesin-2 KIF3AC heterodimer is related to strain-dependent kinetic properties of KIF3A and KIF3C. *Proc. Natl. Acad. Sci. USA.* 117:15632–15641. https://doi.org/10.1073/pnas.1916343117

Brunnbauer, M., F. Mueller-Planitz, S. Kösem, T.H. Ho, R. Dombi, J. Christof, M. Gebhardt, M. Rief, and Z. Ökten. 2010. Regulation of a heterodimeric kinesin-2 through an unprocessive motor domain that is turned processive by its partner. *Proc. Natl. Acad. Sci. USA.* 107:10460–10465. https://doi.org/10.1073/pnas.1005177107

Carpenter, B.S., R.L. Barry, K.J. Verhey, and B.L. Allen. 2015. The heterotrimeric kinesin-2 complex interacts with and regulates GLI protein function. *J. Cell Sci.* 128:1034–1050. https://doi.org/10.1242/jcs.162552

Cole, D.G., S.W. Chinn, K.P. Wedaman, K. Hall, T. Vuong, and J.M. Scholey. 1993. Novel heterotrimeric kinesin-related protein purified from sea urchin eggs. *Nature.* 366:268–270. https://doi.org/10.1038/366268a0

Cole, D.G., D.R. Diener, A.L. Himelblau, P.L. Beech, J.C. Fuster, and J.L. Rosenbaum. 1998. Chlamydomonas kinesin-II-dependent intraflagellar transport (IFT): IFT particles contain proteins required for ciliary assembly in *Caenorhabditis elegans* sensory neurons. *J Cell Biol.* 141:993–1008. https://doi.org/10.1083/jcb.141.4.993

Deeb, S.K., S. Guzik-Lendrum, J.D. Jeffrey, and S.P. Gilbert. 2019. The ability of the kinesin-2 heterodimer kif3AC to navigate microtubule networks is provided by the kif3A motor domain. *J Biol. Chem.* 294:20070–20083. https://doi.org/10.1074/jbc.RA119.010725

Franke, D., and D.I. Svergun. 2009. DAMMIF, a program for rapid ab-initio shape determination in small-angle scattering. *J. Appl. Crystallogr.* 42: 342–346. https://doi.org/10.1107/S0021889809000338

Garbouchian, A., A. Montgomery, S.P. Gilbert, and M. Bentley. 2022. KAP is the neuronal organelle adaptor for kinesin-2 KIF3AB and KIF3AC. *Mol. Biol. Cell.* 33:ar133. https://doi.org/10.1091/MBC.E22-08-0336

Gu, C., W. Zhou, M.A. Puthenveedu, M. Xu, Y.N. Jan, and L.Y. Jan. 2006. The microtubule plus-end tracking protein EB1 is required for Kv1 voltage-gated K+ channel axonal targeting. *Neuron.* 52:803–816. https://doi.org/10.1016/j.neuron.2006.10.022

Gu, Y., and C. Gu. 2010. Dynamics of Kv1 channel transport in axons. *PLoS One.* 5:e11931. https://doi.org/10.1371/journal.pone.0011931

Guzik-Lendrum, S., K.C. Rank, B.M. Bensel, K.C. Taylor, I. Rayment, and S.P. Gilbert. 2015. Kinesin-2 KIF3AC and KIF3AB can drive long-range transport along microtubules. *Biophys. J.* 109:1472–1482. https://doi.org/10.1016/j.bpj.2015.08.004

Heo, S., G.H. Diering, C.H. Na, R.S. Nirujogi, J.L. Bachman, A. Pandey, and R.L. Huganir. 2018. Identification of long-lived synaptic proteins by proteomic analysis of synaptosome protein turnover. *Proc. Natl. Acad. Sci. USA.* 115:E3827–E3836. https://doi.org/10.1073/pnas.1720956115

Hirokawa, N. 1998. Kinesin and dynein superfamily proteins and the mechanism of organelle transport. *Science.* 279:519–526. https://doi.org/10.1126/science.279.5350.519

Hirokawa, N., S. Niwa, and Y. Tanaka. 2010. Molecular motors in neurons: Transport mechanisms and roles in brain function, development, and disease. *Neuron.* 68:610–638. https://doi.org/10.1016/j.neuron.2010.09.039

Hirokawa, N., Y. Noda, Y. Tanaka, and S. Niwa. 2009. Kinesin superfamily motor proteins and intracellular transport. *Nat. Rev. Mol. Cell Biol.* 10:682–696. https://doi.org/10.1038/nrm2774

Hoeprich, G.J., A.R. Thompson, D.P. McVicker, W.O. Hancock, and C.L. Berger. 2014. Kinesin's neck-linker determines its ability to navigate obstacles on the microtubule surface. *Biophys. J.* 106:1691–1700. https://doi.org/10.1016/j.bpj.2014.02.034

Huang, C.J., C.C. Huang, and C.C. Chang. 2012. Association of the testis-specific TRIM/RBCC protein RNF33/TRIM60 with the cytoplasmic motor proteins KIF3A and KIF3B. *Mol. Cell Biochem.* 360:121–131. https://doi.org/10.1007/s11010-011-1050-8

Ichinose, S., T. Ogawa, and N. Hirokawa. 2015. Mechanism of activity-dependent cargo loading via the phosphorylation of KIF3A by PKA and CaMKIIa. *Neuron.* 87:1022–1035. https://doi.org/10.1016/j.neuron.2015.08.008

Ichinose, S., T. Ogawa, X. Jiang, and N. Hirokawa. 2019. The spatiotemporal construction of the axon initial segment via KIF3/KAP3/TRIM46 transport under MARK2 signaling. *Cell Rep.* 28:2413–2426. https://doi.org/10.1016/j.celrep.2019.07.093

Ichinose, S., Y. Susuki, N. Hosoi, R. Kaneko, M. Ebihara, H. Hirai, and H. Iwasaki. 2023. Interaction between Teneurin-2 and microtubules via EB proteins provides a platform for GABAA receptor exocytosis. *Elife.* 12: e83276. https://doi.org/10.7554/eLife.83276

Jiang, R., Q. Feng, D. Nong, Y.J. Kang, D. Sept, and W.O. Hancock. 2025a. Motor clustering enhances kinesin-driven vesicle transport. *Biophys. J.* 124:2033–2040. https://doi.org/10.1016/j.bpj.2025.04.033

Jiang, X., R. Danev, S. Ichinose, B. Niu, S. Ohtsuki, H. Yanagisawa, S. Nagatoishi, K. Tsumoto, N. Hirokawa, and M. Kikkawa. 2025b. The hook-like adaptor and cargo-binding (HAC) domain in the kinesin-2 tail enables adaptor assembly and cargo recognition. *Sci. Adv.* 11:eady5861. https://doi.org/10.1126/sciadv.ady5861

Jiang, X., T. Ogawa, K. Yonezawa, N. Shimizu, S. Ichinose, T. Uchihashi, W. Nagaike, T. Moriya, N. Adachi, M. Kawasaki, et al. 2023. The two-step cargo recognition mechanism of heterotrimeric kinesin. *EMBO Rep.* 24:e56864. https://doi.org/10.15252/embr.202356864

Kikhney, A.G., C.R. Borges, D.S. Molodenskiy, C.M. Jeffries, and D.I. Svergun. 2020. SASBDB: Towards an automatically curated and validated repository for biological scattering data. *Protein Sci.* 29:66–75. https://doi.org/10.1002/pro.3731

Kondo, S., R. Sato-Yoshitake, Y. Noda, H. Aizawa, T. Nakata, Y. Matsuura, and N. Hirokawa. 1994. KIF3A is a new microtubule-based anterograde motor in the nerve axon. *J. Cell Biol.* 125:1095–1107. https://doi.org/10.1083/jcb.125.5.1095

Kumari, N., and S. Yadav. 2019. Modulation of protein oligomerization: An overview. *Prog. Biophys. Mol. Biol.* 149:99–113. https://doi.org/10.1016/j.pbiomolbio.2019.03.003

Liu, C., and J. Luo. 2023. Protein oligomer engineering: A new frontier for studying protein structure, function, and toxicity. *Angew. Chem. Int. Ed. Engl.* 62:e202216480. https://doi.org/10.1002/anie.202216480

Muresan, V., T. Abramson, A. Lyass, D. Winter, E. Porro, F. Hong, N.L. Chamberlin, and B.J. Schnapp. 1998. KIF3C and KIF3A form a novel neuronal heteromeric kinesin that associates with membrane vesicles. *Mol. Biol. Cell.* 9:637–652. https://doi.org/10.1091/mbc.9.3.637

Nakata, T., and N. Hirokawa. 1995. Point mutation of adenosine triphosphate-binding motif generated rigor kinesin that selectively blocks anterograde lysosome membrane transport. *J. Cell Biol.* 131:1039–1053. https://doi.org/10.1083/jcb.131.4.1039

Nishimura, T., K. Kato, T. Yamaguchi, Y. Fukata, S. Ohno, and K. Kaibuchi. 2004. Role of the PAR-3–KIF3 complex in the establishment of neuronal polarity. *Nat. Cell Biol.* 6:328–334. https://doi.org/10.1038/ncb1118

Niu, B., X. Jiang, and M. Kikkawa. 2026. Motor protein tails: Hidden order within disorder. *Mol. Biol. Cell.* 37:pe2. https://doi.org/10.1091/mbc.E25-07-0359

Pesavento, P.A., R.J. Stewart, and L.S.B. Goldstein. 1994. Characterization of the KLP68D kinesin-like protein in *Drosophila*: Possible roles in axonal transport. *J. Cell Biol.* 127:1041–1048. https://doi.org/10.1083/jcb.127.4.1041

Petoukhov, M.V., P. V Konarev, A.G. Kikhney, and D.I. Svergun. 2007. ATSAS 2.1 – Towards automated and web-supported small-angle scattering data analysis. *J. Appl. Crystallogr.* 40:s223–s228. https://doi.org/10.1107/S0021889807002853

Quinn, S.M., D.P. Howsmon, J. Hahn, and S.P. Gilbert. 2018. Kinesin-2 heterodimerization alters entry into a processive run along the microtubule but not stepping within the run. *J. Biol. Chem.* 293:13389–13400. https://doi.org/10.1074/jbc.RA118.002767

Schimert, K.I., B.G. Budaitis, D.N. Reinemann, M.J. Lang, and K.J. Verhey. 2019. Intracellular cargo transport by single-headed kinesin motors. *Proc. Natl. Acad. Sci. USA.* 116:6152–6161. https://doi.org/10.1073/pnas.1817924116

Schindelin, J., I. Arganda-Carreras, E. Frise, V. Kaynig, M. Longair, T. Pietzsch, S. Preibisch, C. Rueden, S. Saalfeld, B. Schmid, et al. 2012. Fiji: An open-source platform for biological-image analysis. *Nat. Methods.* 9:676–682. https://doi.org/10.1038/nmeth.2019

Scholey, J.M. 2013. Kinesin-2: A family of heterotrimeric and homodimeric motors with diverse intracellular transport functions. *Annu. Rev. Cell Dev. Biol.* 29:443–469. https://doi.org/10.1146/annurev-cellbio-101512-122335

Shimizu, N., K. Yatabe, Y. Nagatani, S. Saijyo, T. Kosuge, and N. Igarashi. 2016. Software development for analysis of small-angle x-ray scattering data. *AIP Conf. Proc.* 1471:050017. https://doi.org/10.1063/1.4952937

Signor, D., K.P. Wedaman, L.S. Rose, and J.M. Scholey. 1999. Two heteromeric kinesin complexes in chemosensory neurons and sensory cilia of *Caenorhabditis elegans*. *Mol. Biol. Cell.* 10:345–360. https://doi.org/10.1091/mbc.10.2.345

Svergun, D.I. 1992. Determination of the regularization parameter in indirect-transform methods using perceptual criteria. *J. Appl. Crystallogr.* 25:495–503. https://doi.org/10.1107/S0021889892001663

Teng, J., T. Rai, Y. Tanaka, Y. Takei, T. Nakata, M. Hirasawa, A.B. Kulkarni, and N. Hirokawa. 2005. The KIF3 motor transports N-cadherin and organizes the developing neuroepithelium. *Nat. Cell Biol.* 7:474–482. https://doi.org/10.1038/ncb1249

Vernos, I., J. Heasman, and C. Wylie. 1993. Multiple kinesin-like transcripts in xenopus oocytes. *Dev. Biol.* 157:232–239. https://doi.org/10.1006/dbio.1993.1127

Volkov, V.V., and D.I. Svergun. 2003. Uniqueness of ab initio shape determination in small-angle scattering. *J. Appl. Crystallogr.* 36:860–864. https://doi.org/10.1107/S0021889803000268

Waither, Z., M. Vashishtha, and J.L. Hall. 1994. The Chlamydomonas kinesin-like protein FLA10 is involved in motility associated with the flagellar membrane. *J. Cell Biol.* 126:175–188. https://doi.org/10.1083/jcb.131.6.1517

Webb, S., K. Toropova, A.G. Mukhopadhyay, S.D. Nofal, and A.J. Roberts. 2025. Regulation of kinesin-2 motility by its β-hairpin motif. *Nat. Struct. Mol. Biol.* 32:1989–1998. https://doi.org/10.1038/s41594-025-01630-5

Wedaman, K.P., D.W. Meyer, D.J. Rashid, D.G. Cole, and J.M. Scholey. 1996. Sequence and submolecular localization of the 115-kD accessory subunit of the heterotrimeric kinesin-II (KRP85/95) complex. *J. Cell Biol.* 132:371–380. https://doi.org/10.1083/jcb.132.3.371

Willems, J., A.P.H. de Jong, N. Scheefhals, E. Mertens, L.A.E. Catsburg, R.B. Poorthuis, F. de Winter, J. Verhaagen, F.J. Meye, and H.D. MacGillavry. 2020. Orange: A CRISPR/Cas9-based genome editing toolbox for epitope tagging of endogenous proteins in neurons. *PLoS Biol.* 18:e3000665. https://doi.org/10.1371/journal.pbio.3000665

Yamazaki, H., T. Nakata, Y. Okada, and N. Hirokawa. 1995. KIF3A/B: A heterodimeric kinesin superfamily protein that works as a microtubule plus end-directed motor for membrane organelle transport. *J. Cell Biol.* 130:1387–1399. https://doi.org/10.1083/jcb.130.6.1387

Yamazaki, H., T. Nakata, Y. Okada, and N. Hirokawa. 1996. Cloning and characterization of KAP3: A novel kinesin superfamily-associated protein of KIF3A/3B. *Proc. Natl. Acad. Sci. USA.* 93:8443–8448. https://doi.org/10.1073/pnas.93.16.8443

Yonezawa, K., M. Takahashi, K. Yatabe, Y. Nagatani, and N. Shimizu. 2019. Software for serial data analysis measured by SEC-SAXS/UV-Vis spectroscopy. *AIP Conf. Proc.* 2054:060082. https://doi.org/10.1063/1.5084713

Yonezawa, K., M. Takahashi, K. Yatabe, Y. Nagatani, and N. Shimizu. 2023. MOLASS: Software for automatic processing of matrix data obtained from small-angle X-ray scattering and UV-visible spectroscopy combined with size-exclusion chromatography. *Biophys. Physicobiol.* 20:e200001. https://doi.org/10.2142/biophysico.bppb-v20.0001

Supplemental material

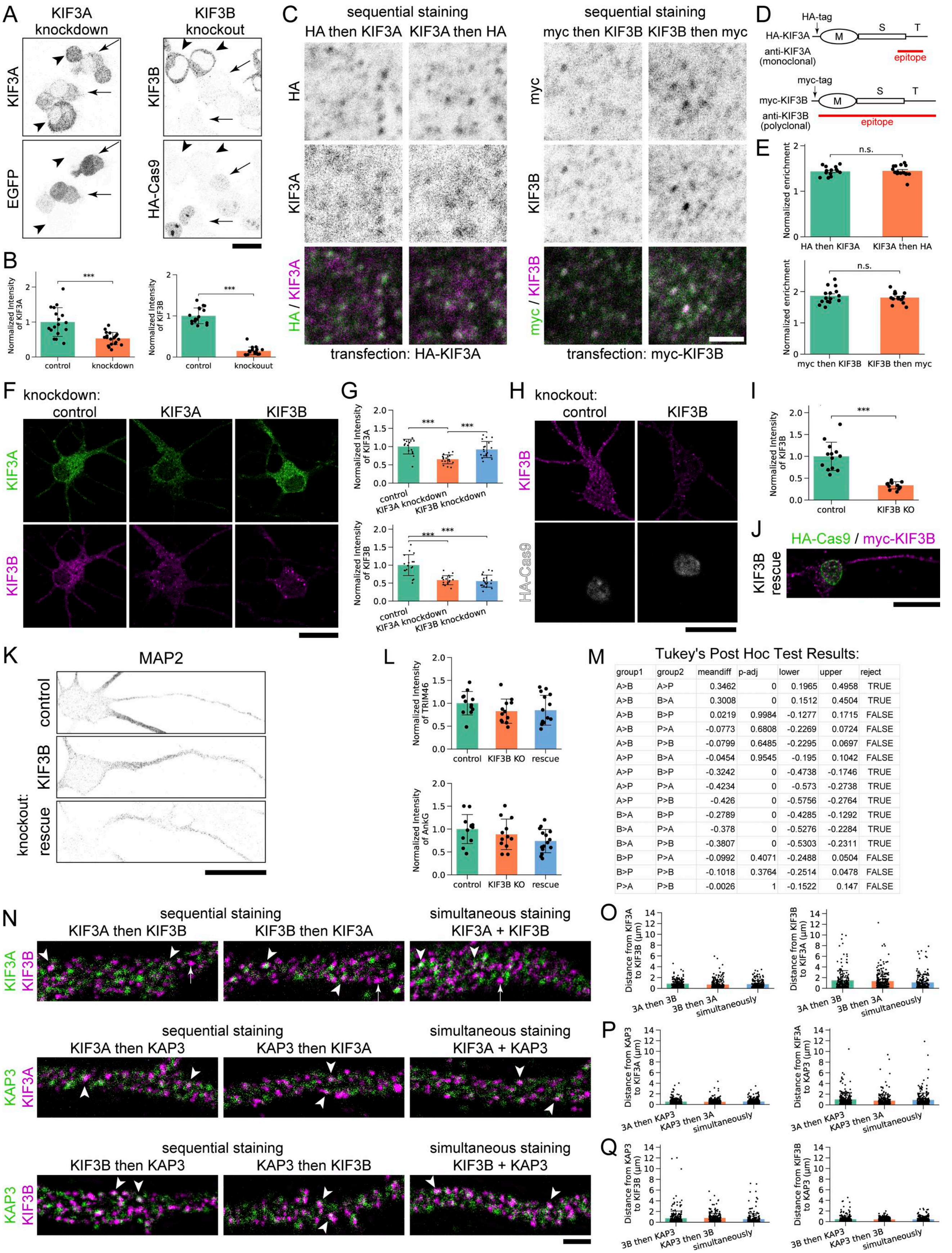

Tukey's Post Hoc Test Results:

group1	group2	meandiff	p-adj	lower	upper	reject
A>B	A>P	0.3462	0	0.1965	0.4958	TRUE
A>B	B>A	0.3008	0	0.1512	0.4504	TRUE
A>B	B>P	0.0219	0.9984	-0.1277	0.1715	FALSE
A>B	P>A	-0.0773	0.6808	-0.2269	0.0724	FALSE
A>B	P>B	-0.0799	0.6485	-0.2295	0.0697	FALSE
A>P	B>A	-0.0454	0.9545	-0.195	0.1042	FALSE
A>P	B>P	-0.3242	0	-0.4738	-0.1746	TRUE
A>P	P>A	-0.4234	0	-0.573	-0.2738	TRUE
A>P	P>B	-0.426	0	-0.5756	-0.2764	TRUE
B>A	B>P	-0.2789	0	-0.4285	-0.1292	TRUE
B>A	P>A	-0.378	0	-0.5276	-0.2284	TRUE
B>A	P>B	-0.3807	0	-0.5303	-0.2311	TRUE
B>P	P>A	-0.0992	0.4071	-0.2488	0.0504	FALSE
B>P	P>B	-0.1018	0.3764	-0.2514	0.0478	FALSE
P>A	P>B	-0.0026	1	-0.1522	0.147	FALSE

Figure S1. **Related to Figs. 1 and 2. (A)** Immunocytochemical validation of anti-KIF3A and anti-KIF3B specificity. Neuro2a cells were transfected with an shRNA vector targeting KIF3A or a CRISPR-Cas9 vector targeting KIF3B and stained with the corresponding antibodies. EGFP and HA-Cas9 were used as transfection markers. Reduced immunoreactivity was observed in transfected cells. Arrows indicate KD or KO cells; arrowheads indicate non-transfected controls. Scale bar, 20 µm. **(B)** Quantification of KIF3A or KIF3B immunofluorescence intensity normalized to the mean of the corresponding control group (set to 1). Data are presented as bar graphs (mean ± SD) with individual data points overlaid. Significant signal reductions were observed in KIF3A KD and KIF3B KO cells (***, $P = 2.54 \times 10^{-4}$ and 2.60×10^{-14} by Welch's *t* test). *n* = 17 and 21 cells (KIF3A control and KD); *n* = 17 and 18 cells (KIF3B control and KO). **(C)** Antigen detection of KIF3 antibodies. Neuro2a cells expressing HA-KIF3A or myc-KIF3B were stained with anti-HA and anti-KIF3A or anti-myc and anti-KIF3B antibodies. Sequential staining was performed in both orders. Punctate KIF3 signals and co-localization were observed under all conditions. Scale bar, 2 µm. **(D)** Schematic of KIF3A and KIF3B constructs and antibody epitopes. HA and myc tags were fused to the N termini of KIF3A and KIF3B, respectively. The anti-KIF3A monoclonal antibody recognizes a region spanning the distal stalk to proximal tail, whereas the anti-KIF3B polyclonal antibody was raised against full-length KIF3B. M, motor; S, stalk; T, tail. **(E)** Quantification of signal enrichment. Data are presented as bar graphs (mean ± SD) with individual data points overlaid. Enrichment of the top 5% KIF3A or KIF3B signal within the top 5% HA or myc regions was quantified and normalized to randomly selected regions. No significant differences were detected between staining orders (n.s., P = 0.768214 and 0.502447 by Welch's *t* test). *n* = 15 cells per condition. **(F)** Immunostaining of KD neurons. KD vectors were electroporated at DIV0, and neurons were immunostained with anti-KIF3A and anti-KIF3B antibodies at DIV4. Scale bar, 20 µm. **(G)** Quantification of KIF3A and KIF3B signal intensity in KD neurons. Data are presented as bar graphs (mean ± SD) with individual data points overlaid. Signal intensities were normalized to the mean intensity of control neurons (set to 1). KIF3A: One-way ANOVA followed by Tukey's post hoc test revealed a significant difference between KIF3A KD and KIF3B KD (***, P = 0.0002), a significant difference between KIF3A KD and control (***, P < 0.0001), and no significant difference between KIF3B KD and control (P = 0.4114). KIF3B: One-way ANOVA followed by Tukey's post hoc test showed no significant difference between KIF3A KD and KIF3B KD (P = 0.9232), while significant differences were observed between KIF3A KD and control (***, P < 0.0001) and between KIF3B KD and control (***, P < 0.0001). *n* = 17 (control), 18 (KIF3A KD), and 19 (KIF3B KD). **(H)** Immunostaining of CRISPR-edited neurons. KO vectors were electroporated at DIV0, and neurons were immunostained with anti-KIF3B and anti-HA antibodies at DIV4. Scale bar, 20 µm. **(I)** Quantification of KIF3B signal intensity in gene-edited neurons. Data are presented as bar graphs (mean ± SD) with individual data points overlaid. ***, $P = 5.47 \times 10^{-6}$ by Welch's *t* test; *n* = 13 (control), 12 (KIF3B KO). **(J)** Immunostaining of rescue experiments. KO vectors together with KO-resistant myc-KIF3B were electroporated at DIV0, and neurons were immunostained with anti-myc and anti-HA antibodies at DIV4 to confirm double-positive cells. Scale bar, 20 µm. **(K)** MAP2 staining of the same neurons shown in Fig. 1 D, confirming neuronal identity and illustrating neurite orientation. **(L)** Quantification of mean intensity per area of TRIM46 and AnkG in the soma. Data are presented as bar graphs (mean ± SD) with individual data points overlaid. No significant differences were detected by one-way ANOVA (P = 0.275 for TRIM46; P = 0.090 for AnkG). *n* = 12 (control), 12 (KIF3B KO), and 15 (rescue). **(M)** Statistical summary for Fig. 2 B. Each row represents a pairwise comparison between two groups. Group 1 and group 2 indicate the compared conditions, and meandiff represents the difference in mean values between group 1 and group 2. P-adj denotes the adjusted P value after correction for multiple comparisons. The lower and upper columns indicate the 95% confidence interval of the mean difference. The reject column indicates whether the null hypothesis was rejected (TRUE, statistically significant difference; FALSE, not significant). Tukey's post hoc analysis showed that A > P and B > A were each significantly different from the remaining groups; however, the difference between A > P and B > A was not statistically significant. **(N)** Immunostaining to assess potential steric interference between antibodies at AIS. To test whether steric hindrance occurs during antibody binding, three staining conditions were performed for the following antibody pairs: KIF3A/KIF3B, KIF3A/KAP3, and KIF3B/KAP3: sequential staining in both orders and simultaneous staining. Arrowheads indicate representative puncta showing co-localized signals; arrows indicate representative puncta positive for KIF3B alone. Scale bar, 2 µm. **(O)** Quantification of the minimum distance from KIF3A to KIF3B and from KIF3B to KIF3A. Data are presented as bar graphs (mean ± SD) with individual data points overlaid. No significant differences were detected among the three staining conditions (from KIF3A to KIF3B: P = 0.0799; from KIF3B to KIF3A: P = 0.0726 by one-way ANOVA). *n* = 18, 25, and 20 cells for the three staining conditions; 10 minimum-distance measurements were randomly sampled per cell. **(P)** Quantification of the minimum distance from KAP3 to KIF3A and from KIF3A to KAP3. Data are presented as bar graphs (mean ± SD) with individual data points overlaid. No significant differences were detected among the three staining conditions (from KAP3 to KIF3A: P = 0.516; from KIF3A to KAP3: P = 0.0964 by one-way ANOVA). *n* = 25, 26, and 25 cells for the three staining conditions; 10 minimum-distance measurements were randomly sampled per cell. **(Q)** Quantification of the minimum distance from KAP3 to KIF3B and from KIF3B to KAP3. Data are presented as bar graphs (mean ± SD) with individual data points overlaid. No significant differences were detected among the three staining conditions (from KAP3 to KIF3B: P = 0.0852; from KIF3B to KAP3: P = 0.216 by one-way ANOVA). *n* = 29, 24, and 26 cells for the three staining conditions; 10 minimum-distance measurements were randomly sampled per cell. In O–Q, 3A and 3B denote KIF3A and KIF3B, respectively.

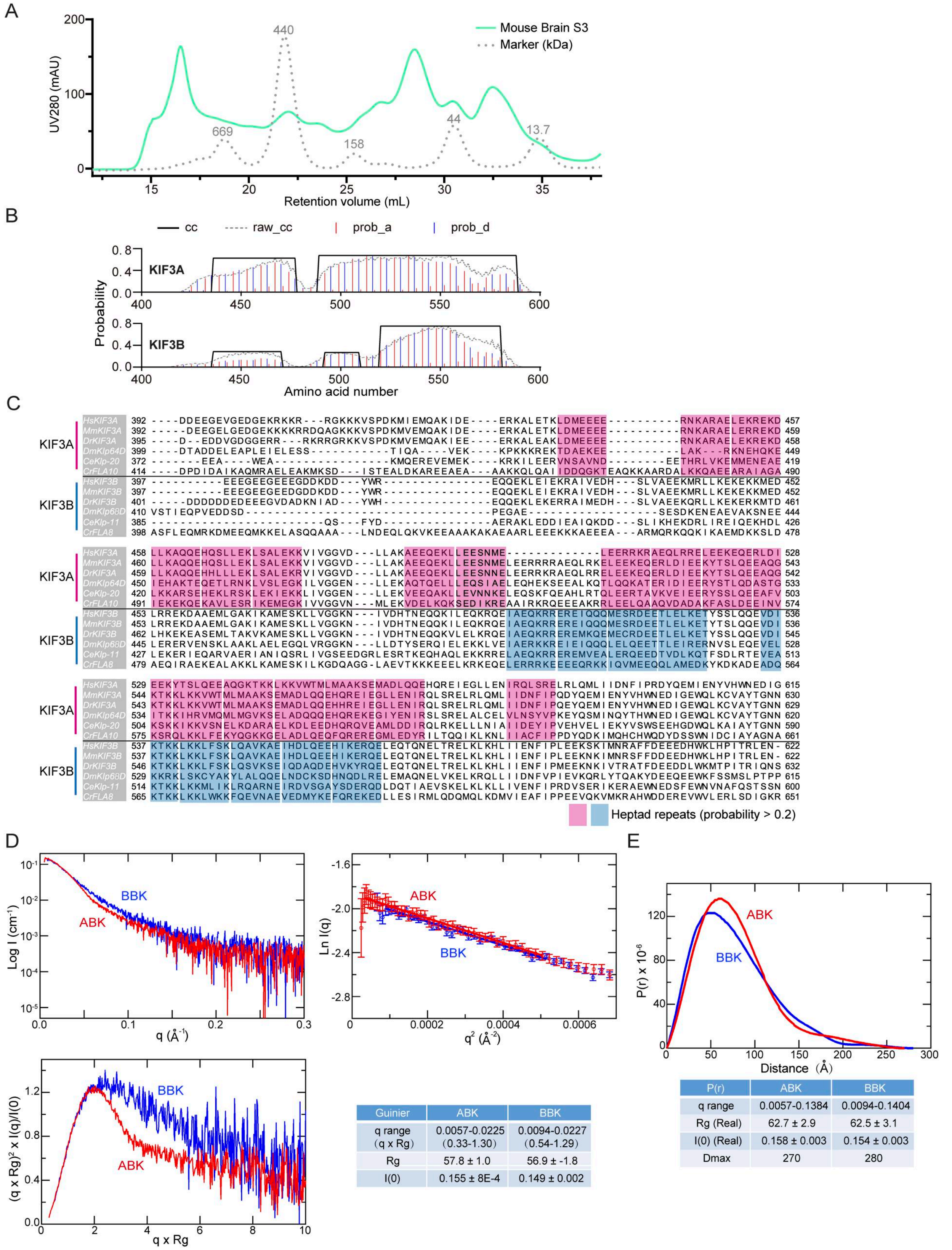

Guinier	ABK	BBK
q range (q x Rg)	0.0057-0.0225 (0.33-1.30)	0.0094-0.0227 (0.54-1.29)
Rg	57.8 ± 1.0	56.9 ± -1.8
I(0)	0.155 ± 8E-4	0.149 ± 0.002

P(r)	ABK	BBK
q range	0.0057-0.1384	0.0094-0.1404
Rg (Real)	62.7 ± 2.9	62.5 ± 3.1
I(0) (Real)	0.158 ± 0.003	0.154 ± 0.003
Dmax	270	280

Figure S2. **Related to Figs. 3, 4 and 5. (A)** HiRes-SEC chromatograph of the mouse brain S3 fraction probing the distribution of KIF3A, KIF3B, KAP3, and TRIM46. **(B)** Prediction of coiled-coil domains of KIF3A/B. cc: sharpened coiled coil propensity; raw_cc: raw coiled coil propensity; prob_a: the probability of a core position; prob_d: the probability of d core position. **(C)** Sequence alignment of the coiled-coil region of KIF3A/B among model organisms. The coiled-coil heptad repeats (with a probability >0.2) are highlighted with a background color. **(D)** Experimental SAXS profiles, Guinier plots, and the statistics of the ABK (in red) and BBK (in blue) complexes. **(E)** Comparison of pair distribution function P(r) of the ABK and BBK.

Provided online is Table S1. Table S1 shows SAXS data collection and analysis statistics.